### Title

The Impact of Surface Structure Transformations on the Performance of Li-Excess Cation-Disordered Rocksalt Cathodes




### Journal

Cell Reports Physical Science, 1(9)

### ISSN

2666-3864



### Authors

Kwon, Deok-Hwang
Lee, Jinhyuk
Artrith, Nongnuch
et al.



### Publication Date

2020-09-01

### DOI

10.1016/j.xcrp.2020.100187

Peer reviewed

Cell Reports
Physical Science

CellPress
OPEN ACCESS

Article

# The Impact of Surface Structure Transformations on the Performance of Li-Excess Cation-Disordered Rocksalt Cathodes

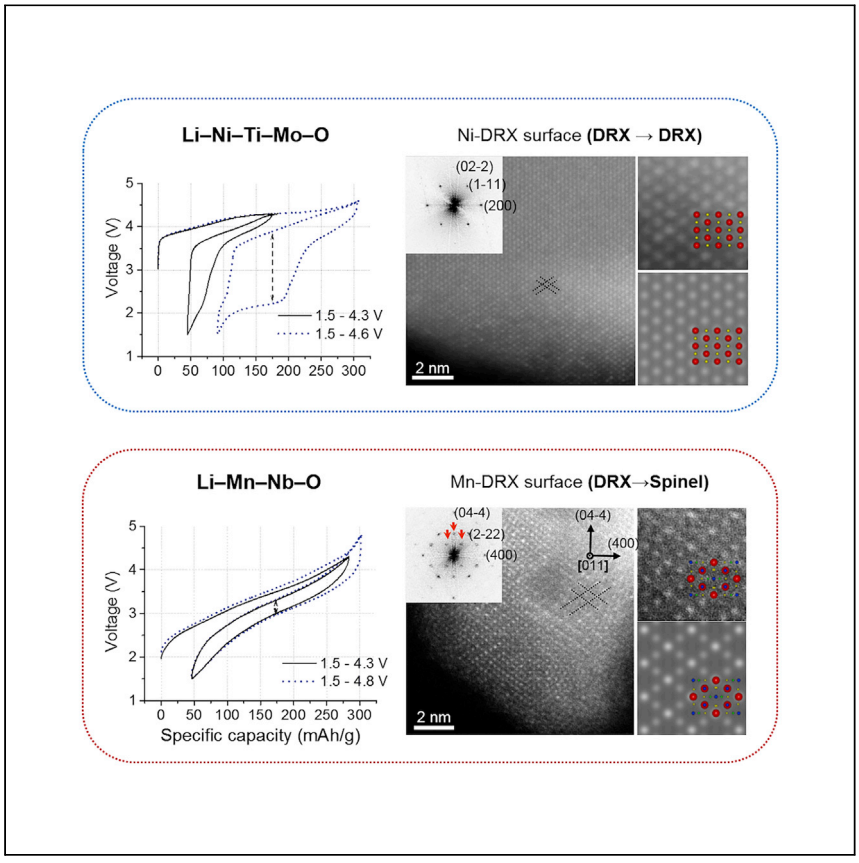


Li-excess cation-disordered rocksalt (DRX) oxides have attracted substantial interest because of their high energy densities. However, the surfaces of DRX cathodes are not thoroughly understood, with severe changes occurring after cycling. Kwon et al. elucidate the effects of surface structure transformations on the electrochemical performance of DRX cathodes.

Deok-Hwang Kwon, Jinhyuk Lee, Nongnuch Artrith, ..., Yaosen Tian, Yimei Zhu, Gerbrand Ceder

dkwon@lbl.gov (D.-H.K.)
gceder@berkeley.edu (G.C.)

## HIGHLIGHTS

Ni- and Mn-based cation-disordered rocksalt (DRX) cathodes are investigated

Ni-based DRX develops a densified DRX surface after oxygen loss

Mn-based DRX develops a densified spinel surface after oxygen loss

Different surface evolutions significantly affect the Li transport properties

Kwon et al., Cell Reports Physical Science *1*, 100187
September 23, 2020
https://doi.org/10.1016/j.xcrp.2020.100187

Cell Reports
Physical Science

CellPress
OPEN ACCESS

Article

# The Impact of Surface Structure Transformations on the Performance of Li-Excess Cation-Disordered Rocksalt Cathodes

Deok-Hwang Kwon,[1,2,5,*] Jinhyuk Lee,[1,2,3,5] Nongnuch Artrith,[1,2] Hyunchul Kim,[2] Lijun Wu,[4] Zhengyan Lun,[1,2] Yaosen Tian,[1,2] Yimei Zhu,[4] and Gerbrand Ceder[1,2,6,*]

## SUMMARY

**Li-excess cation-disordered rocksalt (DRX) oxides have shown potential as high-energy-density Li-ion cathodes. They typically exploit O redox to achieve high capacity, which can trigger oxygen loss at the surface, thereby affecting the cathode performance. Here, we elucidate the impact that the surface structural evolution has on their electrochemical properties by comparing two prototypical DRX cathodes, $Li_{1.2}Ni_{0.333}Ti_{0.333}Mo_{0.133}O_2$ (LNTMO) and $Li_{1.2}Mn_{0.6}Nb_{0.2}O_2$ (LMNO). Both cathodes achieve high capacity, but oxygen loss leads to significant polarization for LNTMO, whereas LMNO is far less affected. We show that while metal densification at the particle surface occurs for both materials, the resulting surface structure is strikingly different. A spinel phase forms at the surface of LMNO, which effectively alleviates oxygen loss and allows fast Li transport, whereas a densified DRX forms at the LNTMO surface, which impedes Li transport and cannot mitigate oxygen loss. These findings demonstrate the importance of the surface structure of DRX cathode.**

## INTRODUCTION

Disordered rocksalt-type (DRX) Li transition metal (TM) oxides have attracted substantial interest as high-energy-density Co-free cathodes for rechargeable Li batteries.[1–9] These materials require Li-excess ($x > 0.1$ in $Li_{1+x}TM_{1-x}O_2$) materials as DRX introduces a percolating network of "0-TM channels" in the structures. $Li^+$ ions can diffuse through these channels without repulsion from high-valent TM ions, resulting in a relatively low Li diffusion barrier for such dense structures.[10]

Many DRX cathodes capable of delivering high capacity (>200 mAh/g) and energy density (>700 Wh/kg) have been developed, including $Li_{1.2}Ni_{0.333}Ti_{0.333}Mo_{0.133}O_2$,[4] $Li_{1.2}Mn_{0.6}Nb_{0.2}O_2$,[3,11] and $Li_2Mn_{2/3}Nb_{1/3}O_2F$,[7] and extensive research has been conducted to understand their underlying electrochemistry and redox mechanism.[8,10,12–17] In particular, the participation of the O anion in the redox process has been intensively investigated,[14,18,19] as the Li excess required to introduce 0-TM percolation limits the traditional TM redox capacity in DRX cathodes. The additional capacity originating from O redox processes in these materials can be substantial. For example, of the ~250 mAh/g initial capacity delivered by $Li_{1.2}Mn_{0.6}Nb_{0.2}O_2$, ~130 mAh/g comes from O redox.[3,11] O redox is facilitated in these materials by the Li excess and disorder[14] or by the vacancies resulting from metal migration,[20] all of which create less bounded O states, which can be more easily oxidized.

[1]Department of Materials Science and Engineering, University of California, Berkeley, Berkeley, CA 94720, USA

[2]Materials Science Division, Lawrence Berkeley National Laboratory, Berkeley, CA 94720, USA

[3]Department of Mining and Materials Engineering, McGill University, Montréal, QC H3A 0C5, Canada

[4]Department of Condensed Matter Physics and Materials Science, Brookhaven National Laboratory, Upton, NY 11973, USA

[5]These authors contributed equally

[6]Lead Contact

*Correspondence: dkwon@lbl.gov (D.-H.K.), gceder@berkeley.edu (G.C.)

https://doi.org/10.1016/j.xcrp.2020.100187

However, there has been some evidence that a large amount of O oxidation can facilitate cation migration and accelerates the loss of oxygen at the surface.[21–23] For layered cathodes, it has been argued that after oxygen loss from the particle surface, undercoordinated cations at the particle surface can diffuse back into the crystal structure to recover their original O coordination. This process necessarily increases the metal contents in the newly developed surface layers (i.e., cation densification).[24–28] For the layered cathodes, these metal-densified layers typically consist of "non-Li-excess" disordered rocksalt and/or "spinel-like" structures,[29–38] although recent work has cast some doubt on the designation of these phases as spinel and rocksalt in Ni-rich oxides.[39,40]

Similar problems are expected for Li-excess DRX cathodes. Recent work has uncovered that the electrochemical performance of some DRX cathodes rapidly degrades after oxygen loss.[3,4,11] One of the prevailing arguments is that the oxygen loss followed by cation densification lowers the Li-excess level at the particle surface to below the percolation threshold of 0-TM channels, resulting in poor Li transport. Thus far, no detailed characterization of the surface structure/composition is available for the DRX cathodes; therefore, the correlation between the surface structure and the performance of the DRX cathodes is still highly unclear.

To understand the changes in surface structure and its effect on the performance of Li-excess DRX cathodes, we combine transmission electron microscopy (TEM), electrochemical tests, and density functional theory (DFT) calculations to directly compare 2 representative Li-excess DRX cathodes, $Li_{1.2}Ni_{0.333}Ti_{0.333}Mo_{0.133}O_2$ (LNTMO)[4] and $Li_{1.2}Mn_{0.6}Nb_{0.2}O_2$ (LMNO).[3,11] Differential electrochemical mass spectrometry has shown that both materials experience oxygen loss in the first charge.[6,9,41] However, the resulting polarization in the voltage curve is significantly smaller for LMNO than for LNTMO, indicating that the consequence of the oxygen loss can be substantially different between different DRX cathodes.

Using scanning TEM (STEM)/electron energy-loss spectroscopy (EELS), high-resolution STEM (HRSTEM) imaging, and electron diffraction, we demonstrate that the surface is metal densified after oxygen loss for both materials; however, a spinel forms on the LMNO particle surface, while the LNTMO surface remains DRX. As the spinel structure enables facile Li diffusion even without excess Li[10] and is resistant to further oxygen loss, Li transport in the surface layers of LMNO is less affected by oxygen loss, and the bulk structure is protected from further oxygen loss. Based on this understanding, we propose design principles to improve the cycling performance of Li-excess cathodes.

## RESULTS

### Synthesis and Electrochemical Properties

LNTMO and LMNO were synthesized using solid-state methods, as described in Method Details. X-ray diffraction (XRD) analysis reveals that both materials form in the disordered rocksalt structure. The indexes of the reflection h k l are all even or all odd numbers, consistent with the face-centered-cubic (FCC) rocksalt structure (space group no. 225, $Fm\bar{3}m$). No secondary phases are detected. The lattice parameters of LNTMO and LMNO are 4.1448 and 4.2205 Å, respectively (Figures 1A and 1B). Detailed refinement information is included in Table S1.

Scanning electron microscopy (SEM) analysis shows different particle size distributions for the two materials. The particle size of the as-made LNTMO is homogeneous

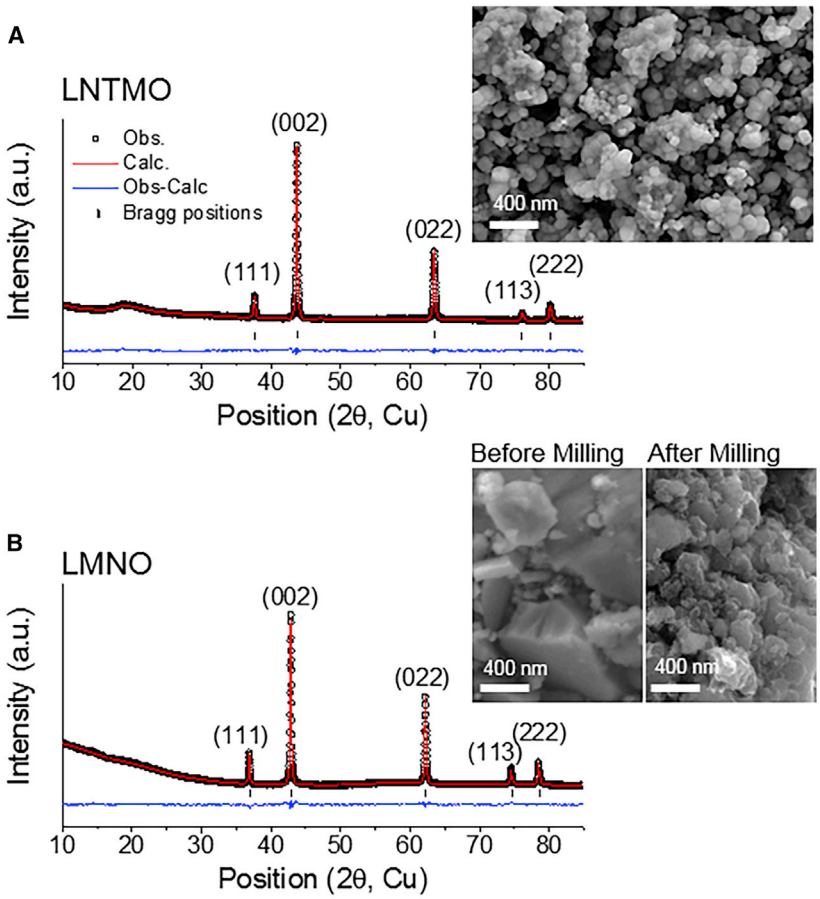


**Figure 1. Characterization of Pristine State LNTMO and LMNO Samples by XRD and SEM**

The X-ray diffraction (XRD) patterns and scanning electron microscopy (SEM) images of (A) $Li_{1.2}Ni_{0.333}Ti_{0.333}Mo_{0.133}O_2$ (LNTMO) and (B) $Li_{1.20}Mn_{0.6}Nb_{0.2}O_2$ (LMNO) (before ball milling). SEM images of LMNO both before and after the ball-milling process.

at ~100 nm (Figure 1A), whereas LMNO has a broad size distribution ranging from tens of nanometers to micrometers (Figure 1B). This difference in the particle size arises because LMNO requires a much higher temperature (1,000°C) to form compared to LNTMO (750°C). Since the performance of the cathode materials can depend on the particle size, we reduced the particle size of LMNO by high-energy ball milling (see Method Details) with carbon black to create a more fair comparison between both materials. The ball milling process results in a more comparable particle size (100–200 nm) of LMNO to that of LNTMO (Figures 1B and S1). A more detailed analysis of the particle-size distribution for LNTMO and LMNO (ball-milled) can be found in Figure S2.

Figures 2A and 2B present the voltage profiles of LNTMO and LMNO when cycled at 20 mA/g. The difference between the charge and discharge curves becomes more significant as the charge cutoff voltage is increased from 4.3 to 4.6 V for LNTMO (Figure 2A) and from 4.3 to 4.8 V for LMNO (Figure 2B). It was previously shown that during the first charge of LNTMO, up to ~120 mAh/g, $Ni^{2+}$ becomes oxidized to ~$Ni^{3+}$, and then O oxidation follows upon charging beyond 4.3 V, which accompanies oxygen loss from the particle surface.[4,6] During discharge, Ni and O reduction occurs with partial Mo reduction at the particle surface, which results in the two-plateau

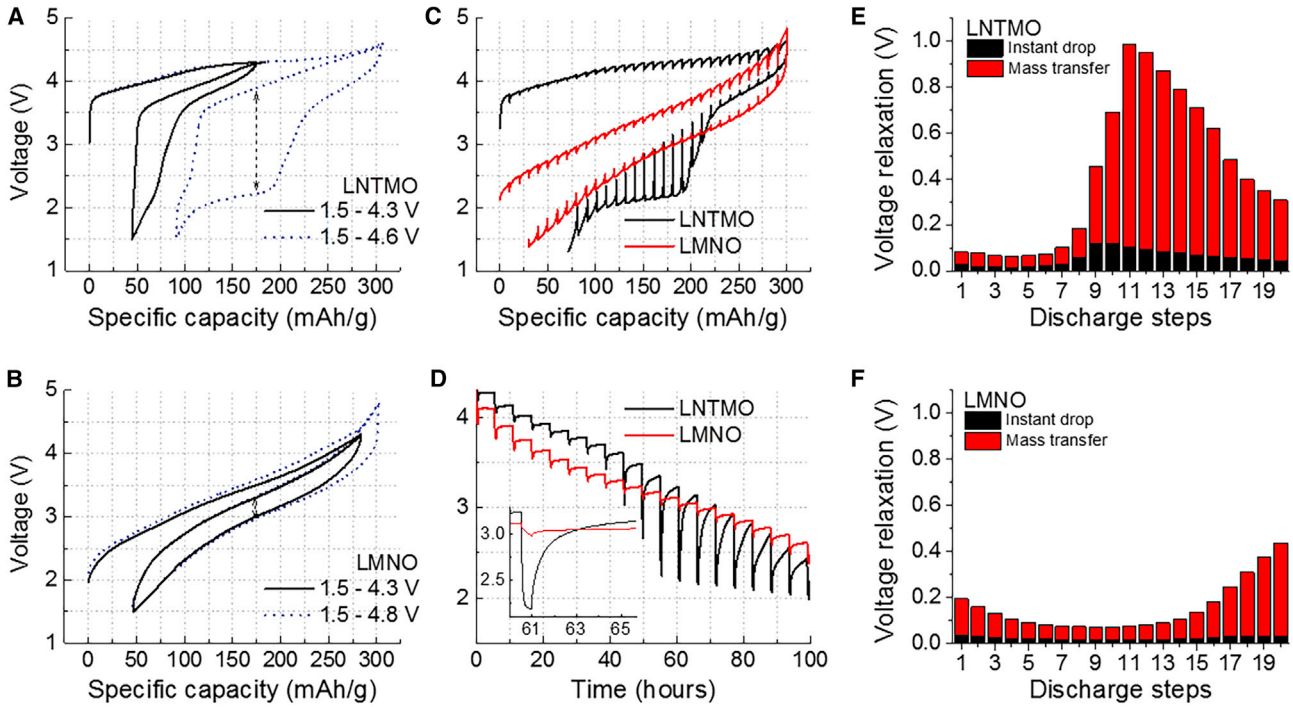


**Figure 2. Electrochemical Tests on LNTMO and LMNO**

(A) The first-cycle voltage profile of LNTMO in the voltage windows of 1.5–4.3 V (black solid) and 1.5–4.6 V (blue dot) (20 mA/g, room temperature).

(B) The first-cycle voltage profile of LMNO in the voltage windows of 1.5–4.3 V (black solid) and 1.5–4.8 V (blue dot) (20 mA/g, room temperature).

(C) The galvanostatic intermittent titration test (GITT) profiles of LNTMO (black) and LMNO (red) during the first charge and discharge, displayed as a function of the specific capacity (20 mA/g, room temperature).

(D) The discharge portion of the GITT profiles displayed as a function of time. The inset focuses on the 60–66 h range.

(E and F) We separate the voltage relaxation during the discharge, which instantly occurs after the current is off (black; IR drop), which occurs slowly over time (red; mass-transfer related resistance) for (E) LNTMO and (F) LMNO.

discharge process widely seen in Ni-based DRX cathodes, such as Li–Ni–Ti–Mo–O or Li–Ni–Nb–O systems (Figure S3).[3,4,6] For LMNO, we previously showed that $Mn^{3+}$/$Mn^{4+}$ oxidation occurs upon first charging to ~170 mAh/g, and further charging involves O oxidation with partial oxygen loss at the surface. Discharging reverses this redox process.[9] We used different voltage cutoffs for the two materials in this test to achieve a similar 1$^{st}$ charge capacity. The increase in the polarization is more substantial for LNTMO than for LMNO. For instance, the voltage difference between the middle of charge and discharge of LNTMO is ~1.5 V after the first charge to 4.6 V, whereas that of LMNO is as low as ~0.3 V (Figures 2A and 2B).

To understand the origin of the voltage hysteresis, we performed the galvanostatic intermittent titration technique (GITT) measurement on the two materials. Figure 2C presents the GITT profiles during the first charge and discharge of LNTMO and LMNO. The LNTMO and LNMO cells were charged to 4.6 and 4.8 V, respectively, and discharged to 1.5 V at 20 mA/g, with a 5-h relaxation step after every 10-mAh/g charge and discharge step. During discharge, the voltage relaxation is significantly higher for LNTMO (close to ~1 V) than for LMNO (~0.2 V). This result indicates poorer kinetics in LNTMO (e.g., slow Li diffusion, high charge transfer resistance) than in LMNO. The voltage relaxation during the titration tests can be divided into two parts: (1) the instant relaxation after the current is off and (2) the slower voltage relaxation afterward (Figures 2D–2F). The former part is related to the charge-transfer resistance or IR drop, while the latter is associated with mass-transfer resistance (Li diffusion). The GITT curves

displayed as a function of time show that the time-dependent portion of voltage relaxation is substantially larger for LNTMO than for LMNO, indicating that the difference in the mass-transfer resistance is the reason why LNTMO shows poorer kinetics (i.e., large polarization) than LMNO.

The electrochemical tests for LMNO, including the GITT, were conducted on the LMNO powder ball milled with C. Thus, the external C layers, as well as reduced particle size, could influence the electrochemical measurements by improving electronic conduction in the cathode film or by reducing the Li diffusion distance. However, the smaller mass-transfer resistance, which we identify as the main reason for the better performance of LMNO compared with LNTMO, is strictly associated with the $Li^+$ ion and polaron conduction "inside" the cathode particles (i.e., Li diffusivity in the crystal structure) and thus is not affected by the external C layers (see also Figures S1D and S1F). In addition, the as-made (not ball milled) LMNO already shows smaller voltage polarization compared with LNTMO (Figure S1). These results suggest that faster Li transport in LMNO compared to LNTMO is intrinsic rather than an effect of ball milling, although the reduced particle size after the ball mill may increase the capacity of LMNO. Note that we cannot completely ignore possible minor changes of the bulk and surface structure by the ball milling. However, no significant changes are detected in the XRD pattern of LMNO after ball milling other than the peak broadening due to the particle size reduction (Figure S1).

The different Li diffusivity in LNTMO and LMNO is also reflected in their rate capability. Figures 3A and 3B show the voltage profiles for LNTMO and LMNO charged and discharged at different rates (20, 50, 100, 200, and 400 mA/g) between 1.5 and 4.6 V for LNTMO and 1.5 and 4.8 V for LMNO, respectively. As the rate increases from 20 to 400 mA/g, the discharge capacity of LNTMO decreases by as much as ~30% from 215 mAh/g to 150 mA/g, while that of LMNO only decreases by ~20% from 255 to 208 mAh/g. We also find that LMNO retains capacity better than LNTMO. Figure 3C compares the capacity retention of LNTMO and LMNO cycled at 100 mA/g. After 100 cycles, 60% and 49% of the initial capacity is retained for LMNO and LNTMO, respectively.

To understand the origin of the different behaviors of the materials, we examined how the structure of the materials changes after cycling. Here, we focus on characterizing the particle surface, where structural and compositional changes due to O redox and oxygen loss are expected to be most severe. Also, the volume fraction of "surface layers" can be significant in the nanoparticles of LNTMO or ball-milled LMNO. Thus, even a small change in the surface layers can substantially influence the performance of the two materials. The effect of bulk structure changes to the performance should be relatively minor, as we argue in the Discussion. To more clearly observe surface changes, we used TEM to compare the surface structure of LNTMO and LMNO at the pristine state and after 20 cycles (at the discharged state). Using well-cycled samples reduces the inhomogeneity among cathode particles with respect to their degree of a reaction, making the TEM result more reliably represent the whole sample. The $20^{th}$-cycle voltage profiles of LNTMO and LMNO are presented in Figure S3.

### Detection of the Metal-Densified Layers and Their Chemical Analysis

We first used STEM/EELS mapping to study how the chemical states of various transition metals in LNTMO and LMNO have changed after 20 cycles, from which we were able to obtain quantitative information about the compositional changes across the particle surface of each material. Figure 4A presents a representative STEM image of the LNTMO particle after cycling; the 2D EEL spectra were recorded

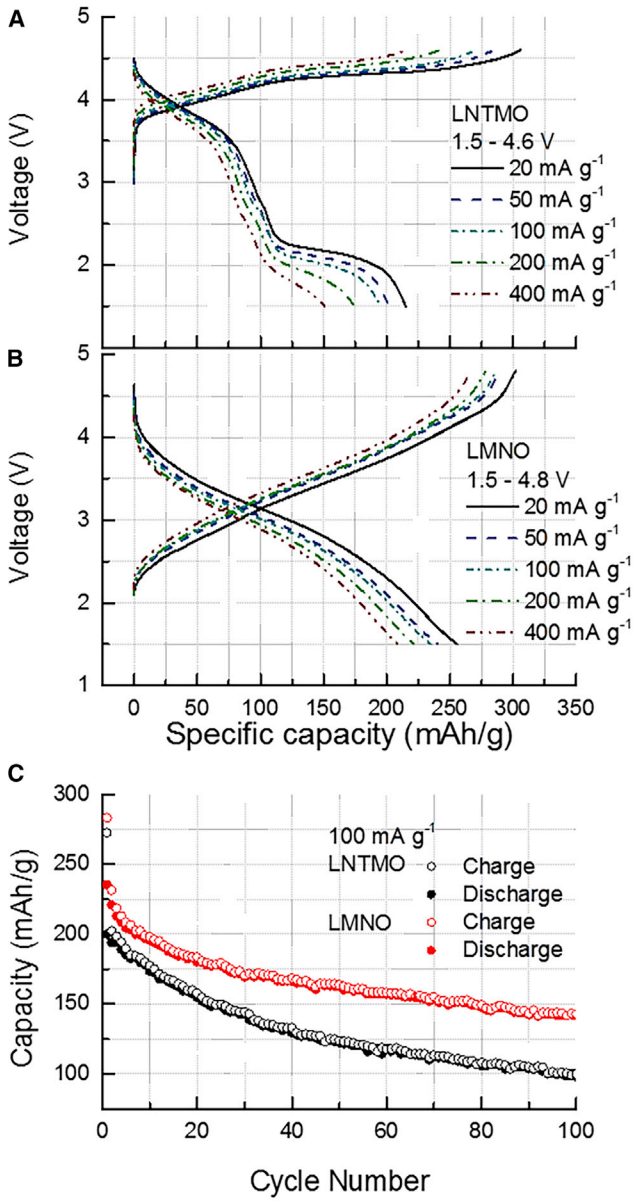


**Figure 3. Rate Performances of LNTMO and LMNO**

(A and B) The voltage profiles of (A) LNTMO and (B) LMNO, when they are charged and discharged at 20, 50, 100, 200, and 400 mA/g (room temperature).

(C) The capacity retention of LNTMO (black) and LMNO (red) when they are cycled at 100 mA/g. In these tests, the voltage window was 1.5–4.6 V for LNTMO and 1.5–4.8 V for LMNO.

from the bulk to the surface (white dotted box). For each pixel of the 2D EEL spectra, the Ni-*L*, Ti-*L*, and O-*K* edges for LNTMO and the Mn-*L* and O-*K* edges for LMNO were recorded. Representative EEL spectra of LNTMO are presented in Figure 4B, where the black, yellow, and red profiles represent the bulk, surface, and outer surface (1–2 nm), respectively.

The oxidation state of a transition metal can be determined from the EELS fine structure.[42] As-synthesized LNTMO contains $Ni^{2+}$, $Ti^{4+}$, and $Mo^{6+}$, as demonstrated by

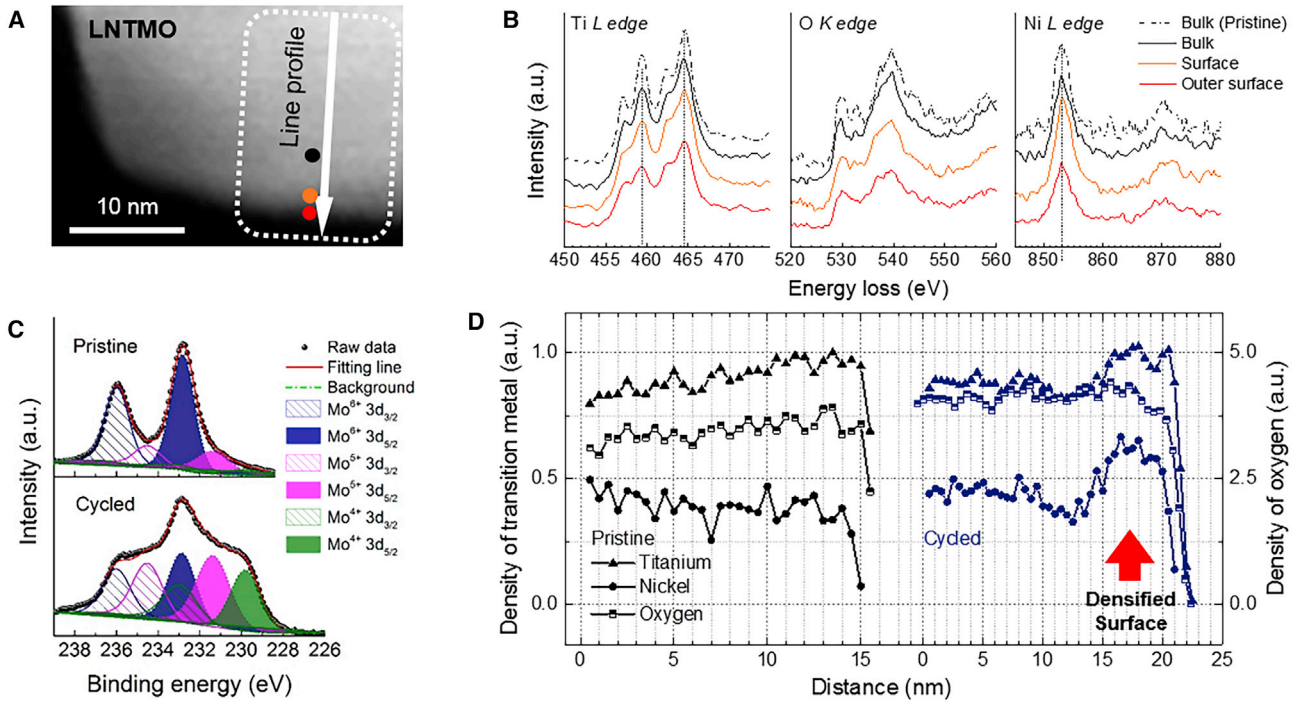


**Figure 4. STEM/EELS and XPS Chemical Analysis on the LNTMO Surface**

(A) The spectrum imaging along the surface of the 20-cycled LNTMO.

(B) Representative EELS spectra (solid profiles) from the regions indicated by the colored circles in (A) and reference EELS from the bulk of the pristine sample (dotted line).

(C) The Mo edge in the XPS spectra collected from the pristine and 20-cycled LNTMO samples.

(D) The volume density of atoms along the surface of the pristine (black) and 20-cycled (blue) LNTMO samples. We quantified the volume density of atoms based on the EELS signals of the O-K edge and Ti- and Ni-L edges. The metal density is indicated on the left y axis and the O density is indicated on the right y axis. The red arrow marks the increased metal density at the surface area.

the EELS and XANES results (Figures S4 and S9). The EELS profile of LNTMO after 20 cycles (Figure 4B) shows that the Ti-*L* and Ni-*L* edge positions remain unchanged from the bulk to the outer surface (black dotted line), indicating that there is no apparent difference of the Ti/Ni oxidation state in the particle surface and core after cycling. Comparing the spectra after cycling with the EELS spectrum from the pristine sample (inserted in Figure 4B as a dotted profile) demonstrates that there is almost no change in the spectra across the cycled surface (see also Figure S4). We assign Ti to be $Ti^{4+}$ as the EELS feature of the Ti-*L* edge shows 4 different peaks with maximum $L_3$ and $L_2$ peak positions at ~459.4 and ~464.6 eV, which are characteristic features of $Ti^{4+}$-containing compounds.[43–45] We assign Ni to be $Ni^{2+}$ based on the maximum peak intensity of the $L_3$ edge at ~853.0 eV.[46,47] $Ni^{3+}$ and $Ni^{4+}$ show a maximum in the $L_3$ edge peak at ~854 and ~856 eV, respectively.[48,49] The intensity of the 2nd peak in the O-*K* edge is slightly smaller in the spectrum collected from the very outer surface (the red profile) than in the one from the bulk (the black profile). This intensity change indicates that there is greater reduction in the metal species at the very outer surface than in the bulk, most likely due to Mo reduction, since Ni and Ti show no evidence of being reduced.

Because Mo is present in small concentrations and gives low signal yield in EELS, the Mo states in LNTMO were measured using X-ray photoelectron spectroscopy (XPS). Figure 4C compares the XPS signal from LNTMO before and after 20 cycles, demonstrating a significant amount of reduction to $Mo^{4+}$ and $Mo^{5+}$ near the particle surface

after cycling. This Mo reduction at the LNTMO particle surface indicates that there was oxygen loss from the material during cycling, which is consistent with differential electrochemical mass spectrometry data reported on this material.[6]

In the literature, it has been argued that the oxygen loss from the particle surface can result in either a structure with O vacancies or a cation-densified structure.[22,50–53] To investigate which structure forms for LMNO and LNTMO, we estimated the volume density of atoms by normalizing the areal density extracted from the STEM/EELS analysis by the thickness (see Method Details). Knowledge of this volume density of atoms enables us to identify whether oxygen loss from the DRX particle surface results in cation densification or leaves O vacancies behind. The relative atomic ratio between metals and O alone cannot differentiate oxygen loss via densification and O vacancies because both processes result in the same atomic ratio between metal and O in the structure.

Figure 4D shows the evolution of the density near the surface of LNTMO after 20 cycles. Figure 4D reveals a substantial increase in the Ni and Ti densities at the surface for ~5 nm by 20%–40% after cycling, whereas the change in the O density is hardly observable. Because of the small Mo content in LNTMO and its low EELS signal yield, we used STEM/energy-dispersive X-ray spectroscopy (EDS) to evaluate the change in the Mo content (Figure S5A), which shows that the Mo content increases similar to Ni and Ti. The increase in TM content at the surface is calculated using the average number of the bulk and surface density from Figure 4D; inherent measurement errors in each number associated with thickness variation and signal-to-noise ratio are canceled out, which results in precision (standard deviation) within <7%.[54]

If oxygen loss were to occur with O vacancies, the O density of the LNTMO surface would be reduced compared with that of the bulk while the cation density would remain unchanged. Instead, we observed a substantial increase in the total TM content at the surface compared with that in bulk, whereas the O content barely changed. This finding indicates that the oxygen loss from LNTMO results in cation densification. According to our quantitative EELS results, we expect that the composition at the surface changes from $Li_{1.2}Ni_{0.333}Ti_{0.333}Mo_{0.133}O_2$ (20% Li excess) to $Li_{0.88}Ni_{0.47}Ti_{0.47}Mo_{0.18}O_2$, (−12% Li excess, 12% TM excess), which is below the threshold Li excess level for 0-TM percolation in the DRX structure.

Based on the smaller voltage polarization observed for LMNO, less densification is expected at the particle surface of LMNO.[6,9,41] We found this expectation to be consistent with our findings. Figure 5 shows the chemical analysis of LMNO before and after 20 cycles. Figure 5A shows a STEM image of an LMNO particle cycled 20 times. The white dotted rectangle indicates where EELS spectra were acquired. A small shift in the Mn-*L* edge of the EELS profile (Figure 5B) to lower energy can be observed at the outer surface (red profile) compared with the bulk (black profile), indicating a slight reduction in Mn. While the Mn-*L* edge appears at ~642.8 eV in the bulk, consistent with $Mn^{3+}$[55] and with the L-edge in the pristine sample (dotted profile in Figures 5B or S4), the chemical shift at the surface indicates a small amount of Mn reduction. After cycling, the O-*K* edge has barely changed other than some narrowing of the first peak in the O-*K* edge, which may arise from the slight reduction in Mn.

The valence state of Nb in LMNO is analyzed using XPS as its low composition makes EELS less sensitive. The XPS data for LMNO (Figure 5C) reveals a slight broadening of the $Nb^{5+}$ 3d peaks; however, no reduced Nb species were detected. These results

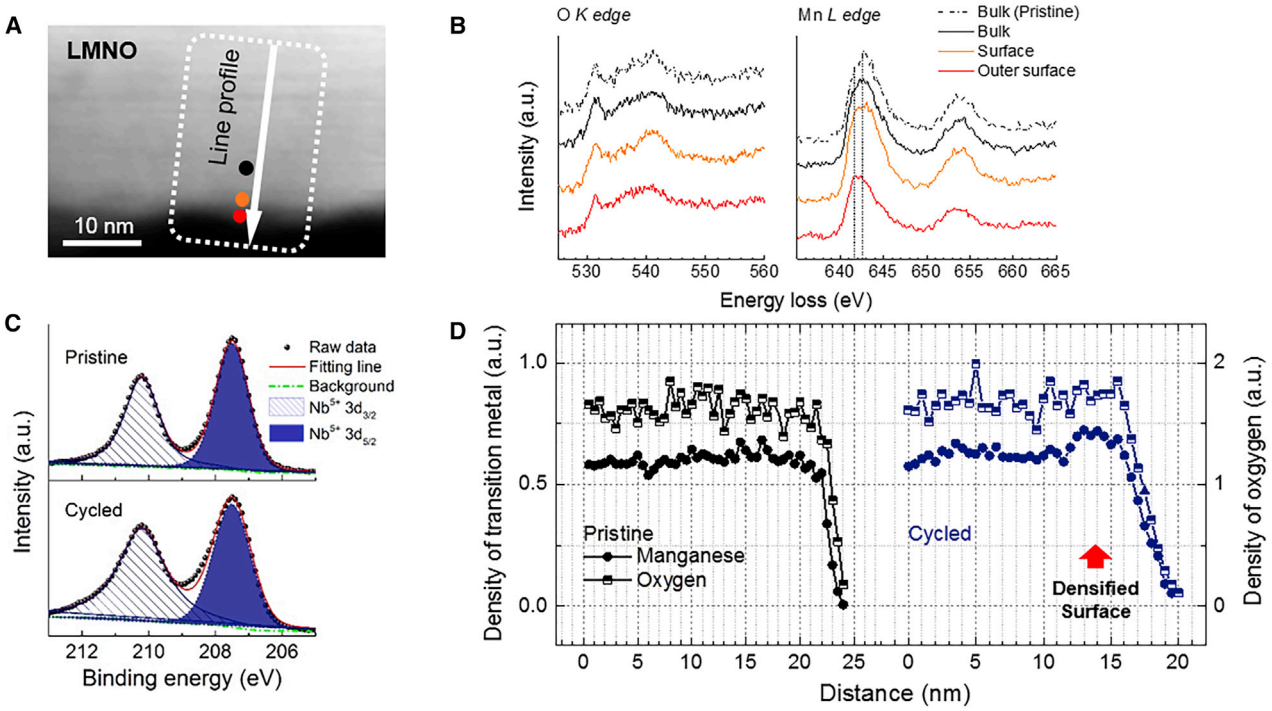


**Figure 5. STEM/EELS and XPS Chemical Analysis on the LMNO Surface**

(A) The spectrum imaging along the surface of the 20-cycled LMNO.

(B) Representative EELS spectra (solid profiles) from the regions indicated by the colored circles in (A) and reference EELS from the bulk of the pristine sample (dotted profiles).

(C) The Nb edge in the XPS spectra collected from the pristine and 20-cycled LMNO samples.

(D) The volume density of atoms along the surface of the pristine (black) and 20-cycled (blue) LMNO samples. We quantified the volume density of atoms based on the EELS signals of the O-K edge and Mn-L edge. The metal density is indicated on the left y axis and the O density is indicated on the right y axis. The red arrow marks the increased metal density at the surface area.

suggest that if Nb reduction occurs in LMNO upon cycling, it is to a much smaller extent than the Mo reduction in LNTMO.

The atomic volume densities of Mn and O near the surface of an LMNO particle before and after cycling are shown in Figure 5D. After 20 cycles, the Mn density increased by ~16% in the ~5 nm region near the surface, whereas the O density did not change much. STEM/EDS analysis reveals that the Nb content increased to an extent similar to that of the Mn content (Figure S5B). From the STEM/EELS and EDS information, we estimate that the composition of LMNO at the surface changes from $Li_{1.2}Mn_{0.6}Nb_{0.2}O_2$ (20% Li excess) to $Li_{1.06-x}Mn_{0.7}Nb_{0.24}O_2$ (6% Li excess) after cycling. This result implies that metal densification also occurred after oxygen loss at the surface of LMNO; however, the degree of densification is smaller than for LNTMO. Nevertheless, 6% Li excess is still below the threshold for 0-TM percolation in the DRX structure; thus, additional explanations are necessary to understand the faster kinetics in LMNO.

## Structure Analysis of Different Phase Transformation at the Surface

To better understand the difference between the two materials, we further investigated the surface structure of the LNTMO and LMNO particles using HRSTEM and electron diffractions. Figure 6A presents HRSTEM images and the corresponding fast Fourier transforms (FFTs) of the surface of an LNTMO particle after 20 cycles

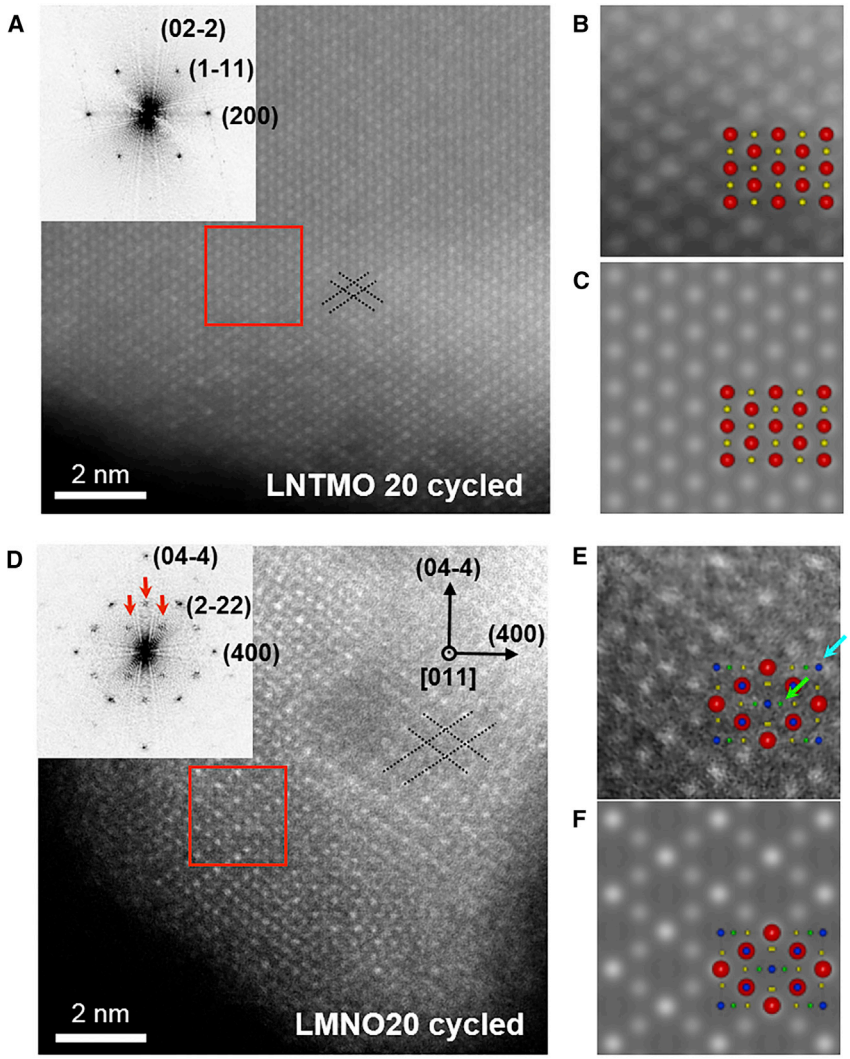


**Figure 6. Atomic-Resolution Images from the Surface of Cycled LNTMO and LMNO**

(A and D) The [011] HRSTEM images of (A) LNTMO and (D) LMNO at the surface of particles after 20 cycles. The insets show the corresponding FFTs of the images, which can be indexed as [011] rocksalt and spinel, respectively. Note that the extra spots (marked by red arrows) in the FFT of (D) are attributed to the spinel structure and are absent in (A).

(B and E) Magnified images from the rectangular areas in (A) and (D).

(C and F) Simulated images obtained using multislice method with frozen phonon approximation for (C) rocksalt structure and (F) spinel structure. The [110] projections of the rocksalt and spinel structures are embedded in the images (red: TMs at 16d site, blue: TMs at 16c site, yellow: O, green: Li)

taken along the [110] direction. There is no contrast modulation of the atomic columns, indicating that a homogeneous DRX surface structure remains after the cycling of LNTMO. This trend is also consistent with the FFT of the HRSTEM image, showing the [110] diffraction pattern of a DRX structure.

In contrast, we observed a distinct phase transformation at the LMNO particle surface after cycling. Figure 6D presents HRSTEM images and FFTs of the surface of an LMNO particle after 20 cycles taken along the [110] direction. An alternating bright contrast of {222} planes (indicated by the black dotted lines) is observed in

the HRSTEM image after cycling (Figure 6D), which is one of the unique features of a spinel structure. The spinel structure has half-occupied and fully occupied TM columns alternating in {222} planes, resulting in the alternation of the contrast of {222} planes. HRSTEM images of pristine LNTMO and LMNO samples are provided in Figure S6.

These HRSTEM images were compared with simulated images to verify the structure and contrast. Magnified HRSTEM images (Figures 6B and 6E) from the marked area (red rectangles in Figures 6A and 6D) are compared with simulated images obtained using the multislice method (Figures 6C and 6F). The [011] projections of the DRX and spinel structures are embedded in the images. Because the contrast of a STEM-high-angle annular dark-field (HAADF) image is approximately proportional to $Z^{1.7}$ (Z is the atomic number)[56] along the atomic column, the light element Li (green spheres) and O (yellow spheres) are invisible in the images. The white dots in the images correspond to the columns of transition metals. The uniform contrast in Figure 6A indicates that Ni, Ti, and Mo (as well as Li in this column) randomly occupy the 4a site in the $Fm\bar{3}m$ space group rocksalt. In the spinel structure ($Fd\bar{3}m$), TMs occupy the 16d site (red spheres in Figures 6E and 6F), while the 16c site (blue spheres) remains unoccupied, resulting in modulating contrast in the HRSTEM image when viewed along the [011] direction.

We note that although the contrast of the HRSTEM images reproduces the spinel structure very well, there is a slight deviation. In an HRSTEM image of a perfect Li–TM–O spinel such as $LiMn_2O_4$, no contrast should be observed at the site indicated by blue arrows in Figure 6E, whereas in our HRSTEM image of LMNO, contrast is observed. This contrast is attributable to the small amount of the remaining DRX structure, which results in background contrast at this site. Also, the weak intensity observable at the Li site (indicated by the green arrow in Figure 6E) of the spinel may infer some occupancy of the tetrahedral site by a TM.[57]

To unambiguously clarify the surface structure of LMNO, we obtained electron diffraction patterns in several different lattice directions (low-index zone axes), [001], [011], and [112], on the particle surface. The crystal symmetry and electron diffraction patterns allow us to differentiate several types of structures (cubic-spinel, tetragonal-spinel, and "spinel-like" structures), which are difficult to distinguish using HRSTEM (HAADF) imaging alone.

The diffraction peaks from the pristine samples (marked by red circles) in Figure 7 correspond to a DRX structure. After 20 cycles, additional diffraction peaks appear in the electron diffraction patterns in the [001], [011], and [112] directions that match well with the simulated diffraction patterns of a cubic-spinel structure (Figures 7D–7F). The systematic extinction rules conclusively verify that the additional peaks correspond to the cubic-spinel structure $Fd\bar{3}m$. Systematic extinctions originate from the combination of the Bravais lattice, screw axis, and glide plane.[58] In the spinel structure, an FCC-type Bravais lattice and a d-glide plane parallel to [001] create the systematic absences. In all of our measured electron diffraction images, the absent diffraction peaks are consistent with these rules for the spinel structure, as indicated by the red triangles in Figure 7. All of the reflections indicate the consistent presence of these components in the electron diffraction patterns, which narrows down the possible symmetry to $Fd\bar{3}$ (203) or $Fd\bar{3}m$ (227). Of these space groups, $Fd\bar{3}m$ is the higher space group, which we can use to represent this structure.

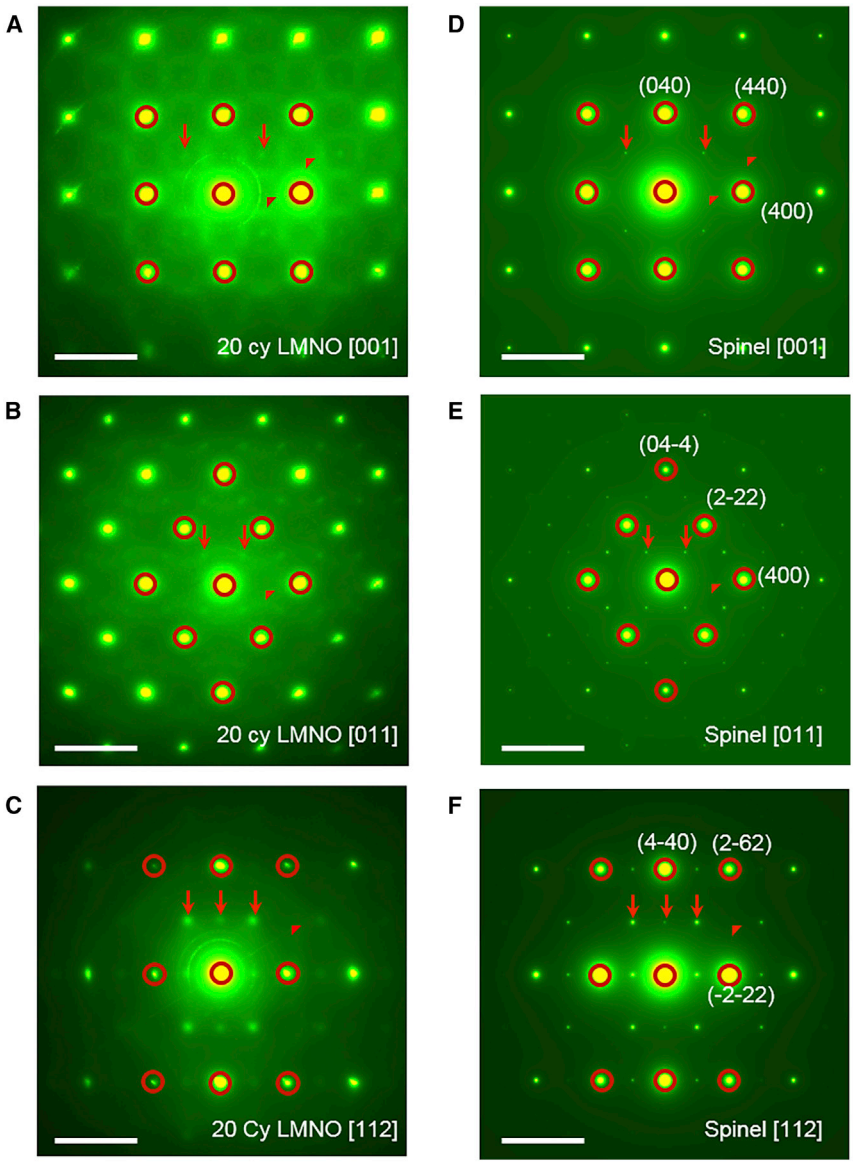


**Figure 7. Electron Diffractions from Cycled LMNO and Simulated Electron Diffractions of Spinel**

The electron diffraction patterns of the 20-cycled LMNO sample in the (A) [001], (B) [011], and (C) [112] directions. We also show the simulated electron diffraction patterns of the modeled cubic-spinel ($LiM_2O_4$ type) structure in the (D) [001], (E) [011], and (F) [112] directions. The red circles indicate the original rocksalt structure; the red arrows mark the extra diffraction peaks that appear after cycling. The red triangles indicate systematic absences of diffraction peaks (scale bar: 0.5 1/nm).

Because LMNO is a relatively Mn-rich compound, both $Mn_3O_4$- and $LiMn_2O_4$-like spinels are candidates for the surface structure of LMNO, as they would show similar TM contrast in HRSTEM images. However, the cubic symmetry observed in the electron diffraction pattern excludes the formation of the $Mn_3O_4$-type spinel, which has tetragonal symmetry. Therefore, we can conclude that a $LiMn_2O_4$-type cubic spinel (e.g., $LiMn_2O_4$, compositionally related spinels such as $Li_4Mn_5O_{12}$[59,60]) formed on the surface of LMNO.

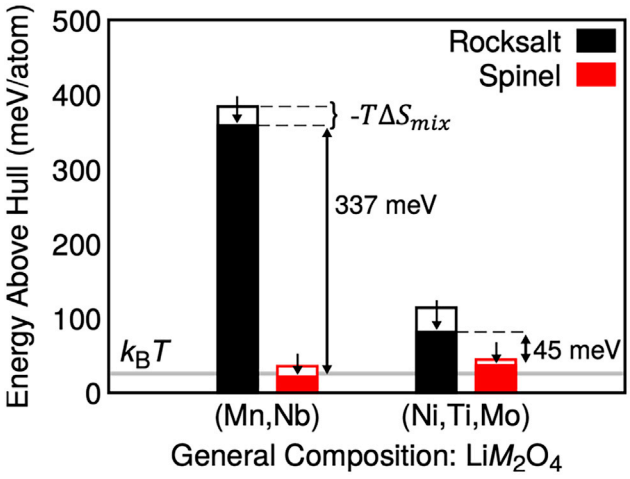


**Figure 8. Formation Energy of Rocksalt and Spinel Structure in LMNO and LNTMO**

Computed formation energies of spinel (red) and rocksalt (black) phases in LNTMO and LMNO. The top of the bars corresponds to the $T = 0$ K DFT formation energies of each structure. At $T = 300$ K, the formation energies are lowered by the entropy of mixing, which is a negative quantity. The magnitude of $-T\Delta S_{mix}$ (shown as empty regions) increases from spinel to rocksalt and from LMNO to LNTMO, owing to the greater number of available sites in rocksalt and chemical species for which mixing occurs (see Method Details).

We also performed electron-diffraction analysis for LNTMO (Figure S7). After 20 cycles, the diffraction pattern remained that of a DRX phase, and no other additional peaks appear. This result indicates that the surface of the LNTMO particles remains cation disordered upon cycling, which is consistent with the HRSTEM image. Note that diffuse scattering in the electron diffraction patterns (Figure 7), indicating short-range ordering, is observed for LMNO but not for LNTMO (Figure S7). Whether short-range ordering is beneficial for transport depends on its specific nature, as has been discussed elsewhere in detail.[61,62]

## Origin of Different Phase Transformation

To understand the origin of the different phase transformation observed from the two materials, we evaluated the relative thermodynamic stability of the spinel and rocksalt-type phase using DFT calculations following a protocol detailed in Method Details. We considered the ideal Li content of the spinel structure ($LiM_2O_4$) to obtain an upper bound for the stabilization of the spinel phase. Note that the $LiM_2O_4$ stoichiometry (M = transition metals with a ratio of Ni:Ti:Mo = 7/15 : 7/15 : 2/16 in LNTMO and of Mn:Nb = 3:1 in LMNO) was used, as it is the closest composition to the one of the metal-densified surface layers (as determined from the quantitative STEM/EELS measurement) that can be accommodated in a manageable unit cell size.

Figure 8 shows the computed formation energies (energies above the ground-state hull) of the most stable rocksalt-type and spinel structures in each compound. In addition to the 0 K DFT energies, Figure 8 also shows the approximate free energy of mixing expected at room temperature obtained by adding the ideal solution entropy of mixing (see Method Details). Li and TM atoms share the same sublattice in the rocksalt phase, such that the entropy of mixing is generally greater than that in the spinel phase. As observed in Figure 8, the formation energy of the spinel phase in the (Mn, Nb) composition is much smaller than that for the rocksalt phase. This

large energy difference leads to a strong driving force for the transition from the rocksalt to the spinel phase for LMNO after metal densification.

For comparison, Figure 8 also shows an equivalent analysis for LNTMO. Here, the energy difference between the rocksalt and spinel phase (45 meV) is significantly smaller. Note that the larger number of TM species in LNTMO than in LMNO directly leads to a greater mixing entropy that helps stabilize the rocksalt phase. Thus, the driving force for a phase transition from the rocksalt to the spinel phase is much smaller for LNTMO than for LMNO.

## DISCUSSION

Using quantitative STEM/EELS analysis, we demonstrated that oxygen loss via metal densification occurs at the surface of both LNTMO and LMNO, but that the degree of metal densification and accompanying structural changes are entirely different for the two materials. We find that the surface structure of LNTMO remains a DRX structure after densification, whereas a cubic spinel is formed at the LMNO particle surface after cycling, as demonstrated by HRSTEM images and electron diffraction patterns. DFT calculations indicate that the different phase transitions can be attributed to the significantly greater energetic preference for the formation of the spinel structure in LMNO than in LNTMO after the oxygen loss.

Using our findings, we are now able to discuss the effect of the different surface structures on the cathode performance. Percolation theory explains that increasing the Li-excess level improves the Li diffusion in the DRX materials, as it enhances the percolating network of the so-called 0-TM channels in their crystal structure.[10] Hence, similar Li diffusivity would be expected for the two materials, as the Li-excess level (20%) is the same for LMNO and LNTMO and is well beyond the 0-TM percolation threshold. When we limit the charge voltage cutoff to 4.3 V, a limited degree of polarization appears in the voltage profile of both LNTMO and LMNO (Figures 2A and 2B), suggesting good Li diffusion in both materials. However, upon high-voltage cycling, we observe that the polarization becomes substantially greater for LNTMO compared with LMNO. In particular, the slowing of Li diffusion in LNTMO is significant during the middle of discharge (Figures 2C–2E). This performance difference can be explained by the different phase evolutions at the surface.

The degree of densification is smaller for LMNO (20% → 6% Li excess) than for LNTMO (20% → −12% Li excess), which suggests that LMNO is less prone to lose oxygen upon high-voltage cycling. The retention of a higher Li-excess content at the surface of LMNO should enable the material to achieve better Li transport.

More important, the spinel formation at the LMNO surface can counteract the adverse effects of cation densification on Li transport. Although high Li excess (>10% Li excess) is crucial for Li percolation in DRX phases, a spinel-like structure does not need Li excess to enable fast Li diffusion.[10] In spinel, Li migrates from one tetrahedral site to another tetrahedral site through an intermediate octahedral site (t-o-t) with a low barrier of ~300 meV.[63,64] Since the 16c site is unoccupied in a spinel, the electrostatic barrier is small when $Li^{1+}$ ions diffuse through the t-o-t channels. Moreover, these channels are connected through a 3-dimensional (3D) network, which has been argued to be related to the good Li mobility in spinel (see also Figure S8).[65,66] Furthermore, overlithiation ($x > 1$ in $Li_xMn_2O_4$) and partial cation disordering so that some of Li atoms occupy the octahedral sites can also enable fast Li diffusion in spinels.[67]

While the smaller amount of oxygen loss from LMNO than from LNTMO may be intrinsic, it is more likely to be a consequence of the high driving force for spinel formation in LMNO. Spinel cathodes, such as $LiMn_2O_4$ and $LiNi_{0.5}Mn_{1.5}O_4$, are known to cycle reversibly at high voltages (even up to 5 V) without a significant loss of oxygen.[68,69] Considering that typical layered or disordered cathodes lose oxygen at above ~4.3 V, the stability of the spinel against oxygen loss is remarkable and is likely due to the tetrahedral site occupancy by Li. The Li-extraction voltage is the sum of the $Li^+$ site energy and the TM oxidation energy.[12,70,71] Because $Li^+$ is more stable in a tetrahedral site (as in spinel) than in an octahedral site (as in rocksalt or layered structure), spinel oxidation voltages are generally higher than in rocksalt or layered phases for the same TM-redox couple. This *de facto* implies that transition metals in a spinel phase at the surface will be less oxidized than in the bulk rocksalt structure, thereby lowering the propensity for oxygen loss.

In contrast, the surface of LNTMO retains the DRX structure during cycling, albeit with declining Li content owing to densification, which will have two effects: (1) Li diffusion will become more difficult upon densification as the Li content drops below the 0-TM percolation threshold of the rocksalt structure and (2) the rocksalt surface phase will be more prone to oxygen oxidation/loss than the spinel phase due to a high population of labile "non-bonding" O 2*p* orbitals in the cation-disordered structure.[14] As the densified disordered surface layer on LNTMO cannot mitigate further oxygen loss, continued oxygen loss will make the surface increasingly more metal densified, leading to poor Li transport through the surface layers (Figures 2 and 3). This phenomenon explains why Ni-based disordered Li-excess cathodes (e.g., Li–Ni–Ti–Mo–O,[4] Li–Ni–Ti–O,[72] Li–Ni–Nb–O[3]) generally cycle with a large polarization, unless oxygen loss is mitigated (e.g., by fluorination).[2,6,9]

We note that compared with LMNO, there is also a more significant change in the bulk structure of LNTMO after cycling, as evidenced by X-ray absorption spectroscopy results (Figure S9). This may have a negative effect on Li diffusion along with surface densification. For instance, it was recently understood that along with the Li-excess level, short-range orderings (SROs) in the DRX oxides could also influence the 0-TM percolation.[62] Nevertheless, no SRO features are seen in the electron diffraction pattern of LNTMO before and after cycling (Figure S7). Without an appearance of any detrimental SRO, the bulk structure change during cycling should result in only a minor impact on the Li diffusion in the DRX oxides.

Our DFT results support the idea that after oxygen loss and metal densification, spinel formation is favored for LMNO but less so in LNTMO. This trend is consistent with data in the literature: (1) the driving force for the spinel transformation becomes most significant when the TM in $LiTM_2O_4$ is Mn[73] and (2) spinel formation in the Mn system is likely further assisted by the fact that $Mn^{3+}$ and $Mn^{2+}$ are mobile in the rocksalt-type structure.[73,74] Reed et al.[73] showed that the half-full *d*-shell (d5: $t_{2g}^3e_g^2$) of $Mn^{2+}$ lowers its energy in a tetrahedral coordination as compared to the other valence states of Mn. As the tetrahedral site is often the activated state for diffusion between octahedral sites, this electronic structure effect increases the Mn mobility in the rocksalt-type structure. $Mn^{3+}$ derives its high mobility by disproportionation into $Mn^{2+}$ as it passes through the tetrahedral site. The high Mn-mobility combined with large thermodynamic driving force toward the spinel structure after oxygen loss explains why the spinel-surface structure develops easily from a variety of Mn-rich cathode materials, including the layered Li- and Mn-rich oxides (e.g., $Li_{1.2}Ni_{0.2}Mn_{0.6}O_2$) after oxygen loss.[75]

In contrast, LNTMO contains $Ti^{4+}$ or $Mo^{6+}$, which are $d^0$ species that can readily accommodate local site distortion induced by cation disordering.[17] $Ni^{2+}$ is also known to cause cation disorder because of its comparable ionic size to $Li^+$, which has been a problem for obtaining well-layered $Ni^{2+}$-based oxides such as $LiNi_{1/2}Mn_{1/2}O_2$[76] and $LiNiO_2$.[77] As these elements lower the energy of the DRX structure, a less driving force for spinel formation exists in LNTMO, making the material highly susceptible to oxygen loss.

Our results indicate that *in situ*/*ex situ* coating of functional layers (i.e., an oxygen -loss-resistive and fast-Li-diffusing layer) would be beneficial for the performance of disordered Li-excess cathode materials. For LMNO, such a layer develops *in situ*, thermodynamically driven by the high content of $Mn^{3+}$ and $Mn^{4+}$. This may explain why Mn-based materials (e.g., $Li_{1.3}Mn_{0.4}Nb_{0.3}O_2$, $Li_2Mn_{2/3}Nb_{1/3}O_2F$, $Li_2Mn_{1/2}Ti_{1/2}O_2F$) have been the most successful disordered cathodes to date.[7,11] It is unfortunate that Ni-based disordered cathodes (Li–Ni–Nb/Ti–O, Li–Ni–Ti–Mo–O) would not develop such an oxygen -loss-resistive spinel layer *in situ*, resulting in more oxygen loss and sluggish Li diffusion. Therefore, preventing oxygen loss by fluorination or *ex situ* coating of a functional layer such as a spinel layer[78–80] could be used to improve the performance of disordered Ni-based cathodes. One would expect to encounter similar problems for Co- or Fe-based DRX cathodes[3,81,82] because their redox behavior is similar to that of Ni—limited TM redox (hardly oxidized to 3+/4+) in DRX due to the significant overlap with O redox and the inability to form a spinel layer *in situ*.

While our work addresses the transformations of the cathode surface, the longer-term cycling of these materials still shows capacity fade (Figure 3C). While it is possible that Mn dissolution from the Mn-rich spinel surface of the LMNO plays a role in this, which is a shared problem of Mn redox-active cathode materials,[83–85] there is also evidence that the 4.8 V charging voltage for LMNO accelerates the electrolyte decomposition.[86,87] Thus, a combined effort to tackle both diffusion-related and non-diffusion-related problems will be critical to developing high-performance DRX cathodes with improved kinetics and cycling stability.

In conclusion, we studied the electrochemical performance and surface phase transformation of two representative Li-excess DRX cathodes, LNTMO and LMNO. Quantitative analysis of the surface layers in both materials revealed that metal densification is less pronounced in LMNO than in LNTMO. In addition, a densified phase with a spinel crystal structure was identified at the surface of LMNO by HRSTEM and electron diffraction. In contrast, the surface structure of LNTMO remains DRX. Our work points to spinel as an ideal surface passivation layer. It facilitates good Li transport and can sustain preferable Li percolation down to low (negative) Li-excess levels. In addition, the low energy for Li in the tetrahedral site reduces its oxidation level and therefore likely also its level of O oxidation, which is consistent with the low level of $O_2$ evolution observed from high-voltage spinels in the literature. Hence, a spinel structure mitigates oxygen loss at the surface and effectively protects the bulk while it maintains good Li diffusion. The different phase evolution at the surface of LNTMO and LMNO results in different polarization.

## EXPERIMENTAL PROCEDURES

### Resource Availability

#### *Lead Contact*

Further information and requests for resources and reagents should be directed to and will be fulfilled by the Lead Contact, Gerbrand Ceder (gceder@berkeley.edu).

*Materials Availability*

All unique and stable reagents generated in this study are available from the Lead Contact upon request.

*Data and Code Availability*

All data associated with the study are included in the article and the Supplemental Information. Additional information is available from the Lead Contact upon reasonable request.

## Synthesis

LNTMO and LMNO materials were synthesized using solid-state synthesis. We used $Li_2CO_3$ (Alfa Aesar, ACS, 99% minimum), $Mn_2O_3$ (Sigma-Aldrich, 99.9%), $Nb_2O_5$ (Sigma-Aldrich, 99.99%), $NiCO_3$ (Alfa Aesar, 99%), $TiO_2$ (Alfa Aesar, 99.9%), and $MoO_2$ (Alfa Aesar, 99%) as precursors. A stoichiometric amount of Li/Ni/Ti precursors were mixed for LNTMO, while a 5% excess amount of Li precursor (and a stoichiometric amount of Mn/Nb precursors) was used for LMNO to compensate for the possible loss of Li during the high-temperature sintering process (1,000°C). The precursor mixing was conducted using wet ball milling with acetone for 24 h, followed by drying overnight in an oven. The precursor mixture was then pelletized and sintered at 750°C for 2 h in the air for LNTMO and at 1,000°C for 1 h under Ar gas flow for LMNO, followed by furnace cooling to room temperature. After the sintering process, we ground the pellets into a powder. For a more fair comparison between LNTMO and LMNO, we reduced the particle size of LMNO using ball milling. We high-energy ball-milled the as-made LMNO powder for 4 h using Retsch PM200 and then shaker milled the high-energy ball-milled LMNO powder with carbon black for 1 h, using the SPEX 800 mixer.

## Electrochemistry

The active material (LMNO or LNTMO), carbon black (Super P, Timcal), and polytetrafluoroethylene (PTFE; Teflon 8C, DuPont) were mixed at a weight ratio of 70:20:10. The mixture was then manually mixed and rolled into a thin film of the composite cathode in an Ar-filled glovebox. The loading of each cathode film was ~4 mg $cm^{-2}$. For the electrolyte, separator, and counter electrode, 1 M $LiPF_6$ in ethylene carbonate (EC) and dimethyl carbonate (DMC) solution (1:1; Techno Semichem), Celgard 2500 polypropylene, and Li-metal foil (FMC) were used, respectively. A total of 2,032 coin cells were assembled inside an Ar-filled glovebox and tested and cycled on an Arbin battery tester using a current of 20 mA/g at room temperature in galvanostatic mode (for voltage profiles). The specific capacity was calculated based on the amount of active material (70 wt%) in the cathode film. We performed GITT during the first charge to 300 mAh/g, followed by discharge to 1.5 V. Every step of 10 mAh/g was galvanostatically charged or discharged at 20 mA/g, followed by relaxing the cell for 5 h between each step.

## Characterization

XRD patterns were collected on a Rigaku MiniFlex diffractometer (Cu source) in the 2θ range of 10°–85°. Rietveld refinement was performed using the PANalytical X'Pert HighScore Plus software. The SEM images were collected on a Zeiss Gemini Ultra-55 analytical field-emission SEM at the Molecular Foundry in the Lawrence Berkeley National Laboratory (LBNL). The XPS measurements were performed on a Thermo Scientific K-Alpha XPS System with a monochromatic Al Ka X-ray source at the Molecular Foundry in LBNL. After galvanostatic cycling 20 times at 20 mA/g, films of LNTMO and LMNO were collected by disassembling the 2,032 coin cells. For comparison, we also conducted the XPS measurement on the pristine

cathode films before cycling. The samples were transferred into the XPS system using a Thermo Scientific KAlpha Vacuum Transfer Module to avoid air exposure, and were cleaned using monoatomic Ar ion milling (1,000 eV, high current mode, 15 s) to remove surface-absorbed C and $O_2$. The spectra Mo and Nb 3d were acquired with a passing energy of 50 eV and a dwell time of 50 ms.

## TEM Characterization

We prepared the pristine and 20-cycled (after the $20^{th}$ discharge) samples of LMNO and LNTMO for TEM characterization. The composite film was sonicated in a diethyl carbonate (DEC) solvent to separate the active material, binder, and carbon black. A few drops of the solvent were drop casted on an ultrathin C grid. To obtain clear HRSTEM images and electron diffraction patterns, unmilled LMNO powders (before and after 20 cycles) were used. TEM experiments were performed at LBNL and at Brookhaven National Laboratory using TEAM 0.5 and JEM-ARM200F, respectively. HRSTEM images were obtained at 200 keV with a convergence angle of ~30 mrad in HAADF mode. STEM/EELS spectra were obtained using a JEM-ARM200F equipped with a GIF Quantum spectrometer using a 22-mrad convergence angle and dispersion of 0.1 (0.25) eV for the LMNO (LNTMO) materials at 200 keV. EELS quantification was performed using a signal integration window of ~50 eV (depending on the element), a Hartree-Slater model of the partial ionization cross-section and power-law background subtraction. To improve the statistical variance of the density number, an averaged line profile was used. The pixel size used in spectrum imaging was ~0.5 Å. The relative thickness was determined by measuring the plasmon intensity in low-loss EEL spectra obtained in dual mode, and it was used to normalize areal density extracted from core-loss EEL spectra to obtain volume density. Electron diffractions were acquired from a whole particle in conventional TEM mode using selected area aperture. Simulated electron diffractions were considered in the bulk particle with the spinel surface of minor disorder using the Bloch wave method.

## X-Ray Absorption Spectroscopy (XAS) Measurements

*Ex situ* XAS measurements were carried out in transmission mode at room temperature using beamline 20-BM at the Advanced Photon Source (APS) of the Argonne National Laboratory (ANL). The prepared XAS samples were sealed with polyimide tape (Kapton, DuPont) to prevent air exposure. The incident energy was selected using a Si(111) monochromator. The incident energy was selected using a Si(111) monochromator, and the beam intensity was reduced by 15% to minimize high-order harmonics using a Rh-coated mirror. Reference spectra of the Ti, Mn, Ni, and Nb metals were collected simultaneously using pure Ti, Mn, Ni, and Nb foils. The XAS data were analyzed using the Athena program, and the spectral energies were calibrated by using the first inflection points in the spectra of Ti, Mn, Ni, and Nb foils. The extracted extended X-ray absorption fine structure (EXAFS) signal, $\chi(k)$, was weighted by $k^3$ to emphasize the high-energy oscillations and then Fourier transformed in a $k$ range from 2.0 to 9.8 Å for the Ti K-edge, from 2.0 to 10.8 Å for the Mn K-edge, from 2.0 to 12.8 Å for the Ni K-edge, and from 2.0 to 9.8 Å for the Nb K-edge using a Hanning window to obtain the magnitude plots of the EXAFS spectra in R-space (Å).

## Calculations

### *DFT*

All of the DFT calculations were performed using the Perdew-Burke-Ernzerhof (PBE) exchange-correlation functional,[88] as implemented in the Vienna *Ab initio* Simulation Package (VASP)[89,90] with projector-augmented wave pseudopotentials.[91] To correct for the DFT self-interaction error, a Hubbard U correction[92–94] was used for Mn (3.9 eV), Ni (6.0 eV), Nb (1.5 eV), and Mo (4.38 eV), with values taken from

Jain et al.[95] The plane-wave cutoff was 520 eV, and the k-point density was selected to be at least 1,000 divided by the number of atoms.[96] The atomic positions and lattice parameters were optimized, and the convergence threshold for the atomic forces was 0.01 eV/Å. The VASP input files were generated using pymatgen.[96]

### *Structure Enumeration*

To determine the most stable 0 K orderings, we systematically enumerated cation configurations in rocksalt and spinel structures with the densified LMNO and LNTMO compositions using the method presented by Hart and coworkers.[97–99] We specifically considered the overall composition $LiM_2O_4$ ($M$ = transition metals)—in other words, the ideal spinel composition. For this composition, the spinel structure is known to be the thermodynamic ground state in many Li-TM oxides,[39,100] such that we could obtain an upper bound of the spinel stabilization.

Densified LMNO was modeled as $LiMn_{1.5}Nb_{0.5}O_4$, with 4 formula units ($Li_4Mn_6Nb_2O_{16}$). To confirm that the selected structure sizes were sufficiently large to find the ground-state energy, we also enumerated the $Li_8Mn_{12}Nb_4O_{32}$ composition in the spinel structure, for which the most stable structure is only ~1 meV per atom more stable, which is not significant for the discussion in the present work. In total, we enumerated ~1,900 spinel and ~1,500 rocksalt configurations, for which all of the subsequent DFT calculations were performed. Densified LNTMO was modeled as $LiNi_{7/8}Ti_{7/8}Mo_{1/4}O_4$, with 8 formula units ($Li_8Ni_7Ti_7Mo_2O_{32}$). Because of the exceedingly large number of possible atomic orderings in rocksalt $Li_8Ni_7Ti_7Mo_2O_{32}$, it was not feasible to enumerate all of the possible configurations in this case. Instead, we enumerated the Li-$M$-vacancy orderings with an anonymous transition metal $M$ and sorted the resulting structures by their electrostatic energy (assuming an average valence state of +3.5 for the $M$ atoms). The most stable configuration was used as a starting point to enumerate the transition metals. This enumeration resulted in >10,000 spinel structures and >10,000 rocksalt structures. To obtain an estimate of the first-principles energetics, we randomly selected ~250 spinel structures and ~250 rocksalt structures for the subsequent DFT calculations.

### *Free Energy of Mixing*

In the ideal disordered $(Li_{0.5}M_{0.5})O$ rocksalt structure, Li and all of the TM species share the same cation sublattice, whereas the Li and TM ions are on different sublattices in the $LiM_2O_4$ spinel structure. Therefore, the entropy of mixing is greater in the rocksalt structure than in the spinel structure. Furthermore, assuming an ideal solution, the mixing entropy in LNTMO is greater than it is in LMNO because of the larger number of chemical species. To estimate the effect of these entropic differences on the energetics in the two systems, we considered the entropy of mixing of the ideal solution[101]:

$$\Delta S_{mix} = -k_B \sum_{i=1}^{N} x_i \ln x_i \,, \qquad \text{(Equation 1)}$$

Where $k_B$ is Boltzmann's constant and $x_i$ is the concentration of species $i$.

## SUPPLEMENTAL INFORMATION

Supplemental Information can be found online at https://doi.org/10.1016/j.xcrp.2020.100187.

## ACKNOWLEDGMENTS

This work was supported by the Assistant Secretary for Energy Efficiency and Renewable Energy, Vehicle Technologies Office, under the Applied Battery Materials

Program, of the US Department of Energy under contract no. DE-AC02-05CH11231. Work at the Molecular Foundry was supported by the Office of Science, Office of Basic Energy Sciences, of the US Department of Energy under contract no. DE-AC02-05CH11231. TEM work at the Brookhaven National Laboratory was supported by the US Department of Energy, Office of Basic Energy Sciences, Division of Materials Science and Engineering, under contract no. DE-SC0012704. The authors would like to thank Dr. Peter Ercius for help with the TEM equipment at the Molecular Foundry.

## AUTHOR CONTRIBUTIONS

D.-H.K. and J.L. developed the project idea. G.C. supervised all aspects of the research. D.-H.K. and J.L. synthesized the proposed compounds and tested and analyzed their electrochemical properties, with help from Z.L. D.-H.K executed the TEM characterization. N.A. performed the DFT calculations and analyzed the results. H.K. conducted the XAS measurements and analyzed the results. L.W. and Y.Z. provided assistance with and advice about the TEM characterization. Y.T. performed the XPS measurements and analyzed the results with H.K. The manuscript was written by J.L. and D.-H.K. and was revised by all of the co-authors. All of the authors contributed to discussions.

## DECLARATION OF INTERESTS

The authors declare no competing interests.

Received: April 6, 2020
Revised: June 26, 2020
Accepted: August 11, 2020
Published: September 16, 2020

## REFERENCES

1. Lee, J., Urban, A., Li, X., Su, D., Hautier, G., and Ceder, G. (2014). Unlocking the potential of cation-disordered oxides for rechargeable lithium batteries. Science *343*, 519–522.
2. Chen, R., Ren, S., Knapp, M., Wang, D., Witter, R., Fichtner, M., and Hahn, H. (2015). Disordered lithium-rich oxyfluoride as a stable host for enhanced $Li^+$ intercalation storage. Adv. Energy Mater. *5*, 1401814.
3. Yabuuchi, N., Takeuchi, M., Nakayama, M., Shiiba, H., Ogawa, M., Nakayama, K., Ohta, T., Endo, D., Ozaki, T., Inamasu, T., et al. (2015). High-capacity electrode materials for rechargeable lithium batteries: $Li_3NbO_4$-based system with cation-disordered rocksalt structure. Proc. Natl. Acad. Sci. USA *112*, 7650–7655.
4. Lee, J., Seo, D.-H., Balasubramanian, M., Twu, N., Li, X., and Ceder, G. (2015). A new class of high capacity cation-disordered oxides for rechargeable lithium batteries: Li–Ni–Ti–Mo oxides. Energy Environ. Sci. *8*, 3255–3265.
5. Freire, M., Kosova, N.V., Jordy, C., Chateigner, D., Lebedev, O.I., Maignan, A., and Pralong, V. (2016). A new active Li-Mn-O compound for high energy density Li-ion batteries. Nat. Mater. *15*, 173–177.
6. Lee, J., Papp, J.K., Clément, R.J., Sallis, S., Kwon, D.-H., Shi, T., Yang, W., McCloskey, B.D., and Ceder, G. (2017). Mitigating oxygen loss to improve the cycling performance of high capacity cation-disordered cathode materials. Nat. Commun. *8*, 981.
7. Lee, J., Kitchaev, D.A., Kwon, D.-H., Lee, C.-W., Papp, J.K., Liu, Y.-S., Lun, Z., Clément, R.J., Shi, T., McCloskey, B.D., et al. (2018). Reversible $Mn^{2+}/Mn^{4+}$ double redox in lithium-excess cathode materials. Nature *556*, 185–190.
8. Kitchaev, D.A., Lun, Z., Richards, W.D., Ji, H., Clément, R.J., Balasubramanian, M., Kwon, D.-H., Dai, K., Papp, J.K., Lei, T., et al. (2018). Design principles for high transition metal capacity in disordered rocksalt Li-ion cathodes. Energy Environ. Sci. *11*, 2159–2171.
9. Lun, Z., Ouyang, B., Kitchaev, D.A., Clément, R.J., Papp, J.K., Balasubramanian, M., Tian, Y., Lei, T., Shi, T., McCloskey, B.D., et al. (2018). Improved Cycling Performance of Li-Excess Cation-Disordered Cathode Materials upon Fluorine Substitution. Adv. Energy Mater. *9*, 1802959.
10. Urban, A., Lee, J., and Ceder, G. (2014). The Configurational Space of Rocksalt-Type Oxides for High-Capacity Lithium Battery Electrodes. Adv. Energy Mater. *4*, 1400478.
11. Wang, R., Li, X., Liu, L., Lee, J., Seo, D.-H., Bo, S.H., Urban, A., and Ceder, G. (2015). A disordered rock-salt Li-excess cathode material with high capacity and substantial oxygen redox activity: $Li_{1.25}Nb_{0.25}Mn_{0.5}O_2$. Electrochem. Commun. *60*, 70–73.
12. Urban, A., Seo, D.-H., and Ceder, G. (2016). Computational understanding of Li-ion batteries. npj Comput. Mater. *2*, 1126.
13. Abdellahi, A., Urban, A., Dacek, S., and Ceder, G. (2016). The Effect of Cation Disorder on the Average Li Intercalation Voltage of Transition-Metal Oxides. Chem. Mater. *28*, 3659–3665.
14. Seo, D.-H., Lee, J., Urban, A., Malik, R., Kang, S., and Ceder, G. (2016). The structural and chemical origin of the oxygen redox activity in layered and cation-disordered Li-excess cathode materials. Nat. Chem. *8*, 692–697.
15. Urban, A., Matts, I., Abdellahi, A., and Ceder, G. (2016). Computational Design and Preparation of Cation-Disordered Oxides for High-Energy-Density Li-Ion Batteries. Adv. Energy Mater. *6*, 1600488.
16. Abdellahi, A., Urban, A., Dacek, S., and Ceder, G. (2016). Understanding the Effect of Cation Disorder on the Voltage Profile of Lithium Transition-Metal Oxides. Chem. Mater. *28*, 5373–5383.
17. Urban, A., Abdellahi, A., Dacek, S., Artrith, N., and Ceder, G. (2017). Electronic-Structure Origin of Cation Disorder in Transition-Metal Oxides. Phys. Rev. Lett. *119*, 176402.

18. Luo, K., Roberts, M.R., Hao, R., Guerrini, N., Pickup, D.M., Liu, Y.-S., Edström, K., Guo, J., Chadwick, A.V., Duda, L.C., and Bruce, P.G. (2016). Charge-compensation in 3*d*-transition-metal-oxide intercalation cathodes through the generation of localized electron holes on oxygen. Nat. Chem. *8*, 684–691.

19. Xu, J., Sun, M., Qiao, R., Renfrew, S.E., Ma, L., Wu, T., Hwang, S., Nordlund, D., Su, D., Amine, K., et al. (2018). Elucidating anionic oxygen activity in lithium-rich layered oxides. Nat. Commun. *9*, 947.

20. Gent, W.E., Lim, K., Liang, Y., Li, Q., Barnes, T., Ahn, S.-J., Stone, K.H., McIntire, M., Hong, J., Song, J.H., et al. (2017). Coupling between oxygen redox and cation migration explains unusual electrochemistry in lithium-rich layered oxides. Nat. Commun. *8*, 2091.

21. Lee, E., and Persson, K.A. (2014). Structural and Chemical Evolution of the Layered Li-Excess $Li_xMnO_3$ as a Function of Li Content from First-Principles Calculations. Adv. Energy Mater. *4*, 1400498.

22. Li, B., and Xia, D. (2017). Anionic Redox in Rechargeable Lithium Batteries. Adv. Mater. *29*, 1701054.

23. Yao, Z., Kim, S., He, J., Hegde, V.I., and Wolverton, C. (2018). Interplay of cation and anion redox in Li4Mn2O5 cathode material and prediction of improved Li4(Mn,M)2O5 electrodes for Li-ion batteries. Sci. Adv. *4*, eaao6754-10.

24. Tran, N., Croguennec, L., Menetrier, M., Weill, F., Biensan, P., Jordy, C., and Delmas, C. (2008). Mechanisms Associated with the "Plateau" Observed at High Voltage for the Overlithiated $Li_{1.12}(Ni_{0.425}Mn_{0.425}Co_{0.15})_{0.88}O_2$ System. Chem. Mater. *20*, 4815–4825.

25. Jung, S.-K., Gwon, H., Hong, J., Park, K.-Y., Seo, D.-H., Kim, H., Hyun, J., Yang, W., and Kang, K. (2013). Understanding the Degradation Mechanisms of $LiNi_{0.5}Co_{0.2}Mn_{0.3}O_2$ Cathode Material in Lithium Ion Batteries. Adv. Energy Mater. *4*, 1300787.

26. Hausbrand, R., Cherkashinin, G., Ehrenberg, H., Gröting, M., Albe, K., Hess, C., and Jaegermann, W. (2015). Fundamental degradation mechanisms of layered oxide Li-ion battery cathode materials: methodology, insights and novel approaches. Mater. Sci. Eng. B *192*, 3–25.

27. Xu, J., Lin, F., Doeff, M.M., and Tong, W. (2017). A review of Ni-based layered oxides for rechargeable Li-ion batteries. J. Mater. Chem. A Mater. Energy Sustain. *5*, 874–901.

28. Nayak, P.K., Erickson, E.M., Schipper, F., Penki, T.R., Munichandraiah, N., Adelhelm, P., Sclar, H., Amalraj, F., Markovsky, B., and Aurbach, D. (2017). Review on Challenges and Recent Advances in the Electrochemical Performance of High Capacity Li- and Mn-Rich Cathode Materials for Li-Ion Batteries. Adv. Energy Mater. *8*, 1702397.

29. Abraham, D.P., Twesten, R.D., Balasubramanian, M., Kropf, J., Fischer, D., McBreen, J., Petrov, I., and Amine, K. (2003). Microscopy and Spectroscopy of Lithium Nickel Oxide-Based Particles Used in High Power Lithium-Ion Cells. J. Electrochem. Soc. *150*, A1450.

30. Wu, L., Nam, K.W., Wang, X., Zhou, Y., Zheng, J.-C., Yang, X.Q., and Zhu, Y. (2011). Structural Origin of Overcharge-Induced Thermal Instability of Ni-Containing Layered-Cathodes for High-Energy-Density Lithium Batteries. Chem. Mater. *23*, 3953–3960.

31. Xu, B., Fell, C.R., Chi, M., and Meng, Y.S. (2011). Identifying surface structural changes in layered Li-excess nickel manganese oxides in high voltage lithium ion batteries: a joint experimental and theoretical study. Energy Environ. Sci. *4*, 2223.

32. Boulineau, A., Simonin, L., Colin, J.-F., Bourbon, C., and Patoux, S. (2013). First evidence of manganese-nickel segregation and densification upon cycling in Li-rich layered oxides for lithium batteries. Nano Lett. *13*, 3857–3863.

33. Lin, F., Markus, I.M., Nordlund, D., Weng, T.C., Asta, M.D., Xin, H.L., and Doeff, M.M. (2014). Surface reconstruction and chemical evolution of stoichiometric layered cathode materials for lithium-ion batteries. Nat. Commun. *5*, 3529.

34. Hwang, S., Chang, W., Kim, S.M., Su, D., Kim, D.H., Lee, J.Y., Chung, K.Y., and Stach, E.A. (2014). Investigation of Changes in the Surface Structure of $Li_xNi_{0.8}Co_{0.15}Al_{0.05}O_2$ Cathode Materials Induced by the Initial Charge. Chem. Mater. *26*, 1084–1092.

35. Shukla, A.K., Ramasse, Q.M., Ophus, C., Duncan, H., Hage, F., and Chen, G. (2015). Unravelling structural ambiguities in lithium- and manganese-rich transition metal oxides. Nat. Commun. *6*, 8711.

36. Yan, P., Zheng, J., Xiao, J., Wang, C.-M., and Zhang, J.-G. (2015). Recent Advances on the Understanding of Structural and Composition Evolution of LMR Cathodes for Li-ion Batteries. Front. Energy Res. *3*, 8694.

37. Mohanty, D., Dahlberg, K., King, D.M., David, L.A., Sefat, A.S., Wood, D.L., Daniel, C., Dhar, S., Mahajan, V., Lee, M., and Albano, F. (2016). Modification of Ni-Rich FCG NMC and NCA Cathodes by Atomic Layer Deposition: Preventing Surface Phase Transitions for High-Voltage Lithium-Ion Batteries. Sci. Rep. *6*, 26532.

38. Sallis, S., Pereira, N., Mukherjee, P., Quackenbush, N.F., Faenza, N., Schlueter, C., Lee, T.L., Yang, W.L., Cosandey, F., Amatucci, G.G., et al. (2016). Surface degradation of $Li_{1-x}Ni_{0.80}Co_{0.15}Al_{0.05}O_2$ cathodes: Correlating charge transfer impedance with surface phase transformations. Appl. Phys. Lett. *108*, 263902.

39. Das, H., Urban, A., Huang, W., and Ceder, G. (2017). First-Principles Simulation of the (Li–Ni–Vacancy)O Phase Diagram and Its Relevance for the Surface Phases in Ni-Rich Li-Ion Cathode Materials. Chem. Mater. *29*, 7840–7851.

40. Xiao, P., Shi, T., Huang, W., and Ceder, G. (2019). Understanding Surface Densified Phases in Ni-Rich Layered Compounds. ACS Energy Lett. *4*, 811–818.

41. Kan, W.H., Chen, D., Papp, J.K., Shukla, A.K., Huq, A., Brown, C.M., McCloskey, B.D., and Chen, G. (2018). Unravelling Solid-State Redox Chemistry in $Li_{1.3}Nb_{0.3}Mn_{0.4}O_2$ Single-Crystal Cathode Material. Chem. Mater. *30*, 1655–1666.

42. Egerton, R. (2011). Electron Energy-Loss Spectroscopy in the Electron Microscope (Springer Science & Business Media).

43. Ohtomo, A., Muller, D.A., Grazul, J.L., and Hwang, H.Y. (2002). Artificial charge-modulation in atomic-scale perovskite titanate superlattices. Nature *419*, 378–380.

44. Muller, D.A., Nakagawa, N., Ohtomo, A., Grazul, J.L., and Hwang, H.Y. (2004). Atomic-scale imaging of nanoengineered oxygen vacancy profiles in $SrTiO_3$. Nature *430*, 657–661.

45. Stoyanov, E., Langenhorst, F., and Steinle-Neumann, G. (2007). The effect of valence state and site geometry on Ti $L_{3,2}$ and O *K* electron energy-loss spectra of $Ti_xO_y$ phases. Am. Mineral. *92*, 577–586.

46. Muller, D.A., and Batson, P.E. (1998). Measurement and models of electron-energy-loss spectroscopy core-level shifts in nickel aluminum intermetallics. Phys. Rev. B Condens. Matter Mater. Phys. *58*, 11970–11981.

47. Potapov, P.L., and Schryvers, D. (2004). Measuring the absolute position of EELS ionisation edges in a TEM. Ultramicroscopy *99*, 73–85.

48. Koyama, Y., Mizoguchi, T., Ikeno, H., and Tanaka, I. (2005). Electronic structure of lithium nickel oxides by electron energy loss spectroscopy. J. Phys. Chem. B *109*, 10749–10755.

49. Ikeno, H., Tanaka, I., Koyama, Y., Mizoguchi, T., and Ogasawara, K. (2005). First-principles multielectron calculations of Ni $L_{2,3}$ NEXAFS and ELNES for $LiNiO_2$ and related compounds. Phys. Rev. B Condens. Matter Mater. Phys. *72*, 075123.

50. Lu, Z., and Dahn, J.R. (2002). Understanding the Anomalous Capacity of $Li/Li[Ni_xLi_{(1/3-2x/3)}Mn_{(2/3-x/3)}]O_2$ Cells Using In Situ X-Ray Diffraction and Electrochemical Studies. J. Electrochem. Soc. *149*, A815–A822.

51. Armstrong, A.R., Holzapfel, M., Novák, P., Johnson, C.S., Kang, S.-H., Thackeray, M.M., and Bruce, P.G. (2006). Demonstrating oxygen loss and associated structural reorganization in the lithium battery cathode $Li[Ni_{0.2}Li_{0.2}Mn_{0.6}]O_2$. J. Am. Chem. Soc. *128*, 8694–8698.

52. Koga, H., Croguennec, L., Mannessiez, P., Ménétrier, M., Weill, F., Bourgeois, L., Duttine, M., Suard, E., and Delmas, C. (2012). $Li_{1.20}Mn_{0.54}Co_{0.13}Ni_{0.13}O_2$ with Different Particle Sizes as Attractive Positive Electrode Materials for Lithium-Ion Batteries: Insights into Their Structure. J. Phys. Chem. C *116*, 13497–13506.

53. Koga, H., Croguennec, L., Menetrier, M., Mannessiez, P., Weill, F., Delmas, C., and Belin, S. (2014). Operando X-ray Absorption Study of the Redox Processes Involved upon Cycling of the Li-Rich Layered Oxide $Li_{1.20}Mn_{0.54}Co_{0.13}Ni_{0.13}O_2$ in Li Ion Batteries. J. Phys. Chem. C *118*, 5700–5709.

54. Leapman, R. (2005). EELS Quantitative Analysis. In Transmission Electron Energy Loss Spectrometry in Materials Science and The EELS Atlas, C.C. Ahn, ed. (Wiley-VCH Verlag GmbH), pp. 49–96.

55. Laffont, L., and Gibot, P. (2010). High resolution electron energy loss spectroscopy of manganese oxides: Application to $Mn_3O_4$ nanoparticles. Mater. Charact. *61*, 1268–1273.

56. Pennycook, S.J., and Nellist, P.D. (2011). Scanning Transmission Electron Microscopy (Springer Science & Business Media).

57. Karim, A., Fosse, S., and Persson, K.A. (2013). Surface structure and equilibrium particle shape of the $LiMn_2O_4$ spinel from first-principles calculations. Phys. Rev. B Condens. Matter Mater. Phys. *87*, 075322.

58. Shmueli, U., Flack, H.D., and Spence, J.C.H. (2016). Methods of space-group determination. In International Tables for Crystallography Space-Group Symmetry, C.P. Brock, T. Hahn, H. Wondratschek, U. Müller, U. Shmueli, E. Prince, A. Authier, V. Kopský, D.B. Litvin, and E. Arnold, et al., eds. (International Union of Crystallography), pp. 107–131.

59. Blasse, G. (1963). The structure of some new mixed metal oxides containing lithium. J. Inorg. Nucl. Chem. *25*, 743–744.

60. Takada, T., Hayakawa, H., and Akiba, E. (1995). Preparation and Crystal Structure Refinement of $Li_4Mn_5O_{12}$ by the Rietveld Method. J. Solid State Chem. *115*, 420–426.

61. Kan, W.H., Deng, B., Xu, Y., Shukla, A.K., Bo, T., Zhang, S., Liu, J., Pianetta, P., Wang, B.-T., Liu, Y., et al. (2018). Understanding the Effect of Local Short-Range Ordering on Lithium Diffusion in $Li_{1.3}Nb_{0.3}Mn_{0.4}O_2$ Single-Crystal Cathode. Chem *4*, 2108–2123.

62. Ji, H., Urban, A., Kitchaev, D.A., Kwon, D.-H., Artrith, N., Ophus, C., Huang, W., Cai, Z., Shi, T., Kim, J.C., et al. (2019). Hidden structural and chemical order controls lithium transport in cation-disordered oxides for rechargeable batteries. Nat. Commun. *10*, 592.

63. Xu, B., and Meng, S. (2010). Factors affecting Li mobility in spinel $LiMn_2O_4$–a first-principles study by GGA and GGA+U methods. J. Power Sources *195*, 4971–4976.

64. Nakayama, M., Kaneko, M., and Wakihara, M. (2012). First-principles study of lithium ion migration in lithium transition metal oxides with spinel structure. Phys. Chem. Chem. Phys. *14*, 13963–13970.

65. Thackeray, M.M., de Picciotto, L.A., de Kock, A., Johnson, P.J., Nicholas, V.A., and Adendorff, K.T. (1987). Spinel Electrodes for Lithium Batteries - A Review. J. Power Sources *21*, 1–8.

66. Thackeray, M.M. (1999). Spinel electrodes for lithium batteries. J. Am. Ceram. Soc. *82*, 3347–3354.

67. Xiao, W., Xin, C., Li, S., Jie, J., Gu, Y., Zheng, J., and Pan, F. (2018). Insight into fast Li diffusion in Li-excess spinel lithium manganese oxide. J. Mater. Chem. A Mater. Energy Sustain. *6*, 9893–9898.

68. Kim, J.H., Myung, S.T., and Sun, Y.K. (2004). Molten salt synthesis of $LiNi_{0.5}Mn_{1.5}O_4$ spinel for 5 V class cathode material of Li-ion secondary battery. Electrochim. Acta *49*, 219–227.

69. Liu, G.Q., Wen, L., and Liu, Y.M. (2010). Spinel $LiNi_{0.5}Mn_{1.5}O_4$ and its derivatives as cathodes for high-voltage Li-ion batteries. J. Solid State Electrochem. *14*, 2191–2202.

70. Aydinol, M., Kohan, A., Ceder, G., Cho, K., and Joannopoulos, J. (1997). Ab initio study of lithium intercalation in metal oxides and metal dichalcogenides. Phys. Rev. B Condens. Matter Mater. Phys. *56*, 1354–1365.

71. Aydinol, M.K., Kohan, A.F., and Ceder, G. (1997). Ab initio calculation of the intercalation voltage of lithium transition metal oxide electrodes for rechargeable batteries. J. Power Sources *68*, 664–668.

72. Liu, Y., Zheng, S., Wan, H., Dou, A., Chu, D., and Su, M. (2017). Synthesis and electrochemical properties of cation-disordered Li-Ni-Ti-O compounds as cathode material for lithium ion batteries. J. Alloys Compd. *728*, 659–668.

73. Reed, J., Ceder, G., and Van Der Ven, A. (2001). Layered-to-Spinel Phase Transition in $Li_xMnO_2$. Electrochem. Solid-State Lett. *4*, https://doi.org/10.1149/1.1368896.

74. Thackeray, M.M. (1997). A Comment on the Structure of Thin-Film $LiMn_2O_4$ Electrodes. J. Electrochem. Soc. *144*, L100.

75. Manthiram, A., Knight, J.C., Myung, S.-T., Oh, S.-M., and Sun, Y.-K. (2015). Nickel-Rich and Lithium-Rich Layered Oxide Cathodes: Progress and Perspectives. Adv. Energy Mater. *6*, 1501010–1501023.

76. Ammundsen, B., and Paulsen, J. (2001). Novel lithium-ion cathode materials based on layered manganese oxides. Adv. Mater. *13*, 943–956.

77. Delmas, C., Pérès, J.P., Rougier, A., Demourgues, A., Weill, F., Chadwick, A., Broussely, M., Perton, F., Biensan, P., and Willmann, P. (1997). On the behavior of the $Li_xNiO_2$ system: an electrochemical and structural overview. J. Power Sources *68*, 120–125.

78. Yu, D.Y.W., Yanagida, K., and Nakamura, H. (2010). Surface Modification of Li-Excess Mn-based Cathode Materials. J. Electrochem. Soc. *157*, A1177–A1182.

79. Song, B., Liu, H., Liu, Z., Xiao, P., Lai, M.O., and Lu, L. (2013). High rate capability caused by surface cubic spinels in Li-rich layer-structured cathodes for Li-ion batteries. Sci. Rep. *3*, 3094.

80. Deng, Y.-P., Yin, Z.-W., Wu, Z.-G., Zhang, S.-J., Fu, F., Zhang, T., Li, J.-T., Huang, L., and Sun, S.-G. (2017). Layered/Spinel Heterostructured and Hierarchical Micro/Nanostructured Li-Rich Cathode Materials with Enhanced Electrochemical Properties for Li-Ion Batteries. ACS Appl. Mater. Interfaces *9*, 21065–21070.

81. Obrovac, M.N., Mao, O., and Dahn, J.R. (1998). Structure and electrochemistry of $LiMO_2$ (M= Ti, Mn, Fe, Co, Ni) prepared by mechanochemical synthesis. Solid State Ion. *112*, 9–19.

82. Glazier, S.L., Li, J., Zhou, J., Bond, T., and Dahn, J.R. (2015). Characterization of Disordered $Li_{(1+\ x)}Ti_{2x}Fe_{(1-3x)}O_2$ as Positive Electrode Materials in Li-Ion Batteries Using Percolation Theory. Chem. Mater. *27*, 7751–7756.

83. Aurbach, D., Markovsky, B., Salitra, G., Markevich, E., Talyossef, Y., Koltypin, M., Nazar, L., Ellis, B., and Kovacheva, D. (2007). Review on electrode–electrolyte solution interactions, related to cathode materials for Li-ion batteries. J. Power Sources *165*, 491–499.

84. Nitta, N., Wu, F., Lee, J.T., and Yushin, G. (2015). Li-ion battery materials: present and future. Mater. Today *18*, 252–264.

85. Zhan, C., Wu, T., Lu, J., and Amine, K. (2018). Dissolution, migration, and deposition of transition metal ions in Li-ion batteries exemplified by Mn-based cathodes – a critical review. Energy Environ. Sci. *11*, 243–257.

86. Edstrom, K., Gustafsson, T., and Thomas, J.O. (2004). The cathode–electrolyte interface in the Li-ion battery. Electrochim. Acta *50*, 397–403.

87. Henschel, J., Peschel, C., Klein, S., Horsthemke, F., Winter, M., and Nowak, S. (2020). Clarification of Decomposition Pathways in a State-of-the-Art Lithium Ion Battery Electrolyte through $^{13}$C-Labeling of Electrolyte Components. Angew. Chem. Int. Ed. Engl. *59*, 6128–6137.

88. Perdew, J.P., Burke, K., and Ernzerhof, M. (1996). Generalized Gradient Approximation Made Simple. Phys. Rev. Lett. *77*, 3865–3868.

89. Kresse, G., and Furthmüller, J. (1996). Efficient iterative schemes for ab initio total-energy calculations using a plane-wave basis set. Phys. Rev. B Condens. Matter *54*, 11169–11186.

90. Kresse, G., and Furthmüller, J. (1996). Efficiency of ab-initio total energy calculations for metals and semiconductors using a plane-wave basis set. Comput. Mater. Sci. *6*, 15–50.

91. Blöchl, P.E. (1994). Projector augmented-wave method. Phys. Rev. B Condens. Matter *50*, 17953–17979.

92. Anisimov, V.I., Zaanen, J., and Andersen, O.K. (1991). Band theory and Mott insulators: Hubbard U instead of Stoner I. Phys. Rev. B Condens. Matter *44*, 943–954.

93. Liechtenstein, A.I., Anisimov, V.I., and Zaanen, J. (1995). Density-functional theory and strong interactions: Orbital ordering in Mott-Hubbard insulators. Phys. Rev. B Condens. Matter *52*, R5467–R5470.

94. Dudarev, S.L., Botton, G.A., Savrasov, S.Y., Humphreys, C.J., and Sutton, A.P. (1998). Electron-energy-loss spectra and the structural stability of nickel oxide: an LSDA+U study. Phys. Rev. B Condens. Matter Mater. Phys. *57*, 1505–1509.

95. Jain, A., Hautier, G., Moore, C.J., Ping Ong, S., Fischer, C.C., Mueller, T., Persson, K.A.,

and Ceder, G. (2011). A high-throughput infrastructure for density functional theory calculations. Comput. Mater. Sci. *50*, 2295–2310.

96. Ong, S.P., Richards, W.D., Jain, A., Hautier, G., Kocher, M., Cholia, S., Gunter, D., Chevrier, V.L., Persson, K.A., and Ceder, G. (2013). Python Materials Genomics (pymatgen): a robust, open-source python library for materials analysis. Comput. Mater. Sci. *68*, 314–319.

97. Hart, G.L.W., and Forcade, R.W. (2008). Algorithm for generating derivative structures. Phys. Rev. B Condens. Matter Mater. Phys. *77*, 224115.

98. Hart, G.L.W., and Forcade, R.W. (2009). Generating derivative structures from multilattices: Algorithm and application to hcp alloys. Phys. Rev. B Condens. Matter Mater. Phys. *80*, 014120.

99. Hart, G.L.W., Nelson, L.J., and Forcade, R.W. (2012). Generating derivative structures at a fixed concentration. Comput. Mater. Sci. *59*, 101–107.

100. Liu, M., Rong, Z., Malik, R., Canepa, P., Jain, A., Ceder, G., and Persson, K.A. (2015). Spinel compounds as multivalent battery cathodes: a systematic evaluation based on ab initio calculations. Energy Environ. Sci. *8*, 964–974.

101. Grandy, W.T. (2008). Entropy and the Time Evolution of Macroscopic Systems (Oxford University Press).